



Simple and fast modelling of radio frequency passives in view of beyond-5G and 6G applications: case study of an RF-MEMS multi-state network described by an equivalent lumped element network

Jacopo Iannacci¹ · Girolamo Tagliapietra¹ · Zlatica Marinković² · Koushik Guha³ · Srinivasa Rao Karumuri⁴ · Irene Dal Chiele⁵ · Massimo Donelli⁵

Received: 7 May 2024 / Accepted: 17 June 2024

© The Author(s), under exclusive licence to Springer-Verlag GmbH Germany, part of Springer Nature 2024

Abstract

The utilization of RF-MEMS, which stands for Microsystem-based (MEMS) Radio Frequency (RF) passive components, is garnering growing attention within the realm of Beyond-5G (B5G) and 6G technologies, despite its longstanding existence. This trend is fueled by the impressive RF characteristics achievable through the judicious exploitation of this technology. However, the complex interplay of various physical phenomena in RF-MEMS, spanning mechanical, electrical, and electromagnetic domains, renders the design and optimization of new configurations challenging. In this study, a modeling approach based on Lumped Element Networks (LEN) is employed to accurately predict the Scattering Parameters (S-parameters) characteristics of multi-state and highly reconfigurable RF-MEMS devices. The device under scrutiny is a multi-state RF step power attenuator, previously fabricated, tested, and documented in literature by the principal author. Although these physical devices exhibit flat attenuation characteristics, they are subject to certain non-idealities inherent to the technology. The refined LEN-based methodology presented herein aims to interpret and incorporate such undesirable parasitic effects to provide precise predictions for real RF-MEMS devices. Two custom metrics, referred to as Percent Magnitude Difference (PMD) and Percent Phase Difference (PPD), are utilized to evaluate the accuracy of the LEN model, revealing differences consistently within 1 and 8%, respectively, across a frequency range spanning from 100 MHz to 13.5 GHz.

1 Introduction

The investigation and documentation of Microsystem-based devices (MEMS) for fabricating miniaturized Radio Frequency (RF) passive components have been ongoing for

a considerable period. This effort has led to the development of RF-MEMS technology, which has been extensively explored and documented (Yao 2000; Brown 1997, 1998; Goldsmith et al. 1998; Pillans et al. 1999; Malczewski et al. 1999; Shen and Feng 1999). RF-MEMS has been utilized in mass-market products for several years, with smartphones being among the foremost adopters (Iannacci 2015). Beyond this conventional application, the remarkable RF performance of RF-MEMS, coupled with their substantial reconfigurability and design flexibility, as well as relatively low manufacturing costs, position such a solution as a Key Enabling Technology (KET) for advancing mobile communication beyond the 5th generation (B5G), into 6G and Future Networks (FN), particularly targeting operation in the sub-THz range (100–300 GHz) and beyond (Iannacci 2022; Oberhammer 2017; Shah et al. 2017, 2015).

A pivotal phase in the development of innovative RF-MEMS devices involves modeling, as optimizing their characteristics entails navigating a plethora of Degrees of

✉ Jacopo Iannacci
iannacci@fbk.eu

¹ Center for Sensors and Devices (SD), Fondazione Bruno Kessler (FBK), 38123 Trento, Italy

² Faculty of Electronic Engineering, University of Niš, 18000 Niš, Serbia

³ Department of Electronics and Communication Engineering, National Institute of Technology (NIT) Silchar, Silchar, Assam 788010, India

⁴ Department of Electronics and Communication Engineering, Koneru Lakshmaiah University, Guntur 522502, India

⁵ Department of Civil, Environmental and Mechanical Engineering – DICAM, University of Trento, 38123 Trento, Italy

Freedom (DoF), encompassing both technological and geometrical aspects. This turns into addressing numerous trade-offs, often spanning across different physical domains. Indeed, the multi-physical nature of MEMS-based RF passive components steps across mechanical, electromechanical, and electromagnetic characteristics (Uttamchandani 2013; Gad-el-Hak 2001; Tilli et al. 2015), which frequently interact with each other, complicating the optimization process.

When analyzing the RF and electromagnetic properties of RF-MEMS, a prevalent approach involves constructing a Lumped Element Network (LEN), incorporating resistors, capacitors, and inductors to accurately replicate S-parameter characteristics over a defined frequency range (Yammouch et al. 2008; Patrick Yue and Simon Wong 2000). While LEN-based models may offer less flexibility compared to full 3D analyses based on the Finite Element Method (FEM), they can achieve high levels of accuracy with significantly lower computational demands. Targeting this requires a foundation of robust physical principles when structuring the network architecture and selecting appropriate values for each lumped element (Marcelli et al. 2004; Iannacci et al. 2010a).

Within such context, this study focuses on refining a LEN model describing the RF behavior of a complex RF-MEMS device, specifically a multi-state reconfigurable step power attenuator. The study is arranged according to this structure: following the current introductory Sect. 1, Sect. 2 elaborates on the design concept and operational principles of the RF-MEMS power attenuator in question. Section 3 delves into the specifics of the LEN model, while Sect. 4 addresses the experimental behavior of the network and verifies the accuracy of the LEN model. Finally, Sect. 5 presents concluding remarks.

2 RF-MEMS step power attenuator design concept

The reconfigurable MEMS-based RF step power attenuator examined in this study was initially introduced in (Iannacci et al. 2010b, 2011) and is manufactured using the RF-MEMS surface micromachining technology platform documented in Giacomozzi et al. (2011). The fundamental device is integrated within a Coplanar Waveguide (CPW) structure, with the RF signal divided into two parallel sections. Attenuation of the RF signal is achieved through resistive loads positioned along the line, which are composed of a polycrystalline silicon layer passivated with oxide. RF-MEMS series ohmic switches actuated electrostatically are employed to either select or short the resistors loading the RF line, thus adjusting the resulting attenuation

level. A visual depiction of the physical sample is presented in Fig. 1.

The in-plane dimensions of the whole network in Fig. 1 are $1370\ \mu\text{m}$ along the x-axis and $2200\ \mu\text{m}$ along the y-axis. Concerning the CPW structure, the RF ground planes are $1020\ \mu\text{m}$, while the RF line and gap width are both equal to $50\ \mu\text{m}$. Focusing on the RF-MEMS switches employed in the design, each micro-relay is $90\ \mu\text{m}$ (x-axis) by $250\ \mu\text{m}$ (y-axis).

As previously outlined, the RF line undergoes a bifurcation into two parallel segments upon reaching the input termination of the network, before being recombined at the output. This division is facilitated by four RF-MEMS series ohmic switches assigned to each branch. In the initial segment, denoted as Section A in Fig. 1, two series micro-relays provide independent control. In their default state (OFF), these switches disconnect their corresponding branches (OPEN), whereas upon activation (ON), the branches are inserted (CLOSE). Specifically, the upper branch is governed by the micro-relay A_u , while the lower branch is managed by A_d . Consequently, with neither relay engaged, the entire network remains open. Conversely, the activation of either relay loads one branch of the RF line,

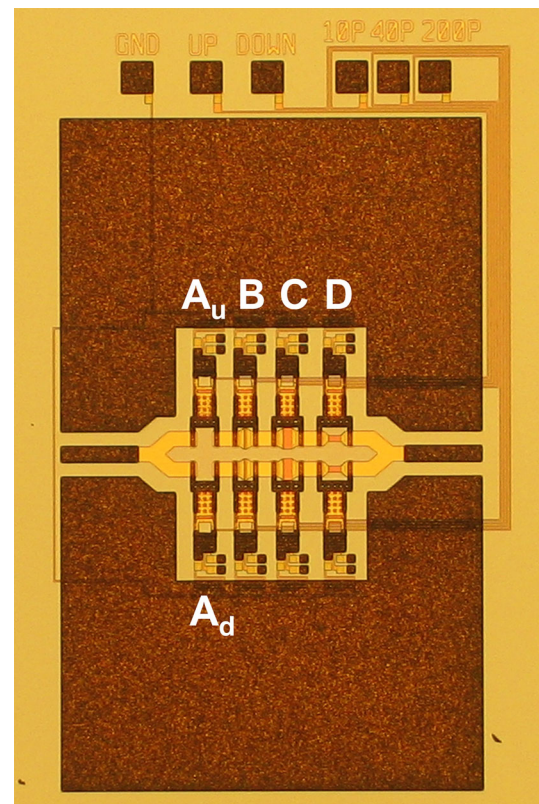


Fig. 1 Microphotograph of the RF-MEMS multi-state attenuator discussed in (Iannacci et al. 2010b, 2011) with the micro-switches-operated reconfigurable stages highlighted

while the simultaneous activation of both A_u and A_d connects the two lines in parallel.

Moving beyond Section A, the upper and lower switches of Sections B, C, and D lack independent control, as their biasing lines are interconnected. Within each of these sections resides a polycrystalline silicon resistor of distinct value. Activation of one or more switches within Sections B, C, or D results in the shorting of the corresponding resistor(s), thereby diminishing the total attenuation imposed by the network. These three sections collectively offer eight distinct levels of attenuation, which, when combined with the various configurations enabled by A_u and A_d , yield a total of 16 different operational states. A detailed 3D close-up of Sections B, C, and D is depicted in Fig. 2, providing insight into the intricate design and layout of these components.

The three resistive loads are labelled as R_{LB} , R_{LC} , R_{LD} , and will be discussed with more details in the next section.

3 Lumped Element Network (LEN) model

The development of the Lumped Element Network (LEN) architecture predicting the RF characteristics of the RF-MEMS multi-state power attenuator builds upon research conducted by the primary author, as documented in Iannacci et al. 2010b; Iannacci et al. 2011; Iannacci et al. 2009). This innovative approach gathers methodologies delineated in prior works, consolidating insights garnered from studies conducted at the elemental device level to construct a comprehensive model of the network. By synthesizing concepts and techniques reported in the mentioned publications, the current study endeavors to provide a holistic depiction of the complex behavior exhibited by the RF-MEMS attenuator.

A pivotal aspect involves the incorporation of an intrinsic attenuator endowed with switchable resistive

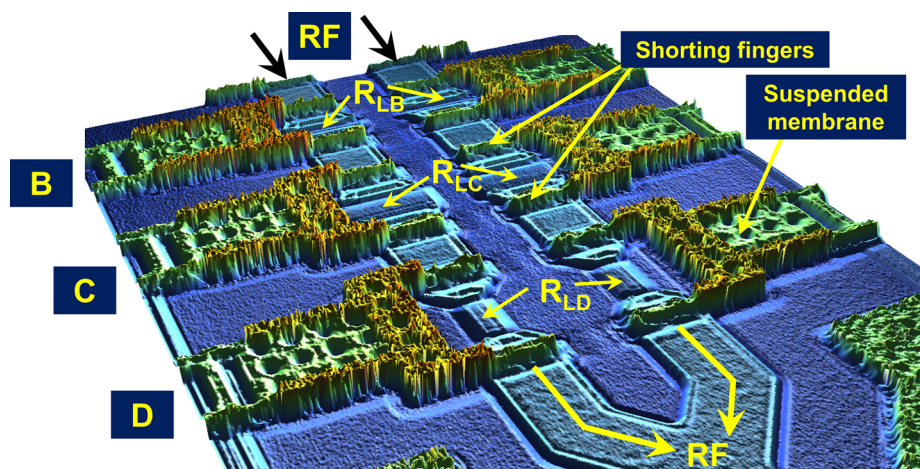
loads. Here, a shorting resistor operates in parallel to the primary load, remaining deactivated (OPEN) when the load is intended to be introduced onto the RF line. This configuration enables dynamic management of the attenuator, facilitating precise control over signal attenuation levels while ensuring optimal performance across a spectrum of operating conditions.

The overall network is sketched in the schematic depiction of the complete LEN, showcased in Fig. 3. This comprehensive illustration serves as a visual guide, elucidating the interconnected components and pathways that collectively govern the behavior of the RF-MEMS multi-state power attenuator within the LEN framework. By leveraging insights from prior research and pioneering methodologies, the LEN architecture represents a significant advancement in the realm of RF network modeling, offering a versatile platform for exploring and optimizing the performance of next-generation communication systems.

The network architecture comprises distinct components, including CPW (Coplanar Waveguide) and vertical via sections, characterized by specular configurations at both input and output terminations, alongside an intrinsic attenuator segment. Detailed insights into the CPW and vertical via sections are available in the close-up depiction presented in Fig. 4, offering a comprehensive view of their design and layout. These sections play a pivotal role in facilitating signal propagation and ensuring impedance matching within the network structure.

Additionally, the intrinsic attenuator section embodies a critical aspect of the network, enabling dynamic control over signal attenuation levels to accommodate varying operational requirements. By integrating a combination of lumped components, the attenuator section affords precise management of signal attenuation while maintaining signal integrity and fidelity.

Fig. 2 Measured 3D profile (white-light interferometer) of the B, C, D sections of the RF-MEMS attenuator in Fig. 1



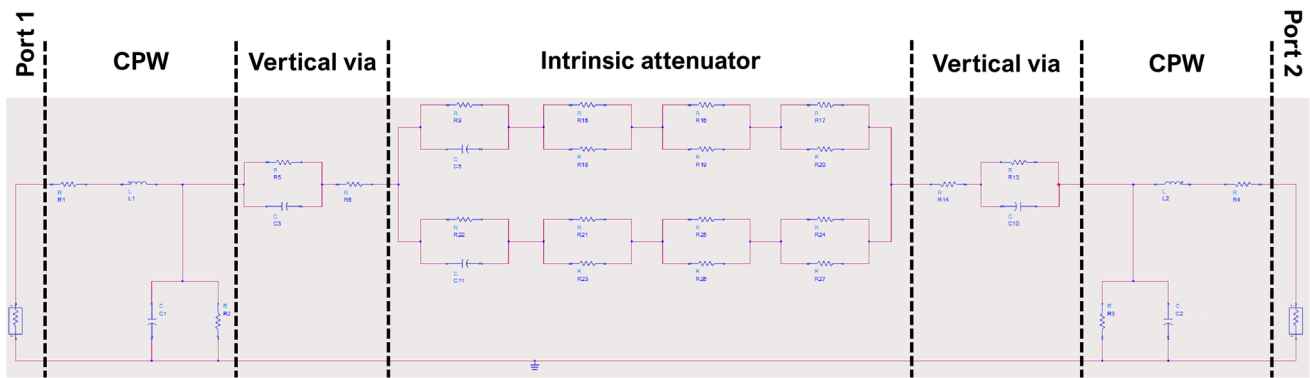
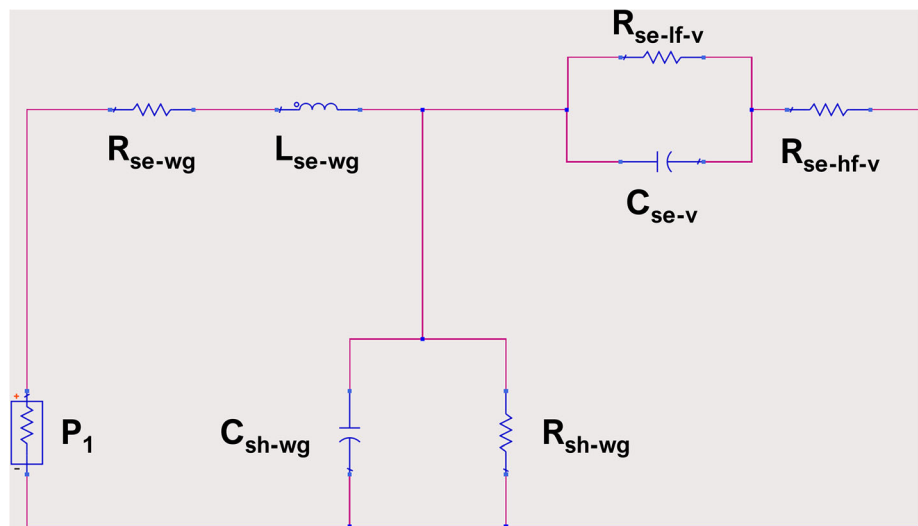


Fig. 3 Complete LEN schematic describing the RF characteristics of the attenuator in Fig. 1

Fig. 4 Close-up of the input CPW section and vertical via section, the latter modelling the contact non-idealities due to technology spreads. The output CPW and vertical via sections are identical and simply mirrored



Furthermore, the nomenclature, description, and optimal extracted values of each lumped component incorporated within the LEN framework are listed in Table 1. This comprehensive tabulation serves as a reference, providing

essential insights into the constituent elements that collectively contribute to the functionality and performance of the network.

Table 1 List of the lumped elements included in the LEN shown in Figs. 3, 4, 5

Element	[Section]—description	Value
R_{se-wg}	[CPW]—series resistance of the line	1 Ω
L_{se-wg}	[CPW]—series inductance of the line	250 pH
C_{sh-wg}	[CPW]—shunt capacitive coupling of the line	10 fF
R_{sh-wg}	[CPW]—shunt resistive loss of the line	1 G Ω
C_{se-v}	[Vertical via]—series parasitic capacitance of the unwanted titanium oxide layer over vias	5 pF
$R_{se-lf-v}$	[Vertical via]—series resistive loss of the unwanted titanium oxide layer over vias	25 Ω
$R_{se-hf-v}$	[Vertical via]—series parasitic resistance of the unwanted titanium oxide layer over vias	5 Ω
$R_{se-sw-cl}$	[Attenuator]—ON state series resistance of the RF-MEMS switch (CLOSE configuration)	1 Ω
$C_{se-sw-op}$	[Attenuator]—OFF state series capacitance of the RF-MEMS switch (OPEN configuration)	10 fF
R_{LB}	[Attenuator]—resistive load of section B	29 Ω
R_{LC}	[Attenuator]—resistive load of section C	116 Ω
R_{LD}	[Attenuator]—resistive load of section D	580 Ω

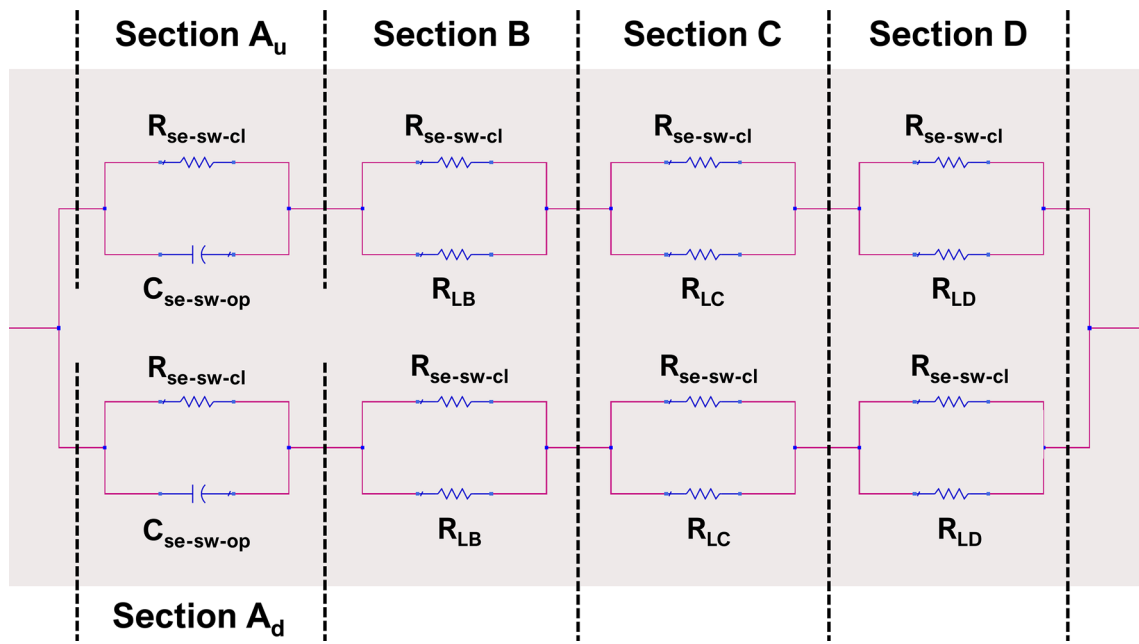


Fig. 5 Close-up of the intrinsic attenuator sections A (split into A_u and A_d), B, C, D

By leveraging these detailed specifications and design considerations, engineers and researchers can gain a deeper understanding of the network architecture and its underlying principles. Such insights are instrumental in optimizing performance, refining design parameters, and advancing the capabilities of RF-MEMS multi-state power attenuators for diverse applications in communication systems and beyond.

The CPW (Coplanar Waveguide) section within the network architecture serves to emulate the behavior of the input and output lines of the RF-MEMS attenuator depicted in Fig. 1. Employing a classical lumped-element approach, this section incorporates series and shunt resistive and reactive components to accurately capture the electrical characteristics of the RF signal propagation. Such modeling techniques have been extensively discussed in prior literature, providing a robust framework for characterizing transmission line behavior.

Conversely, the vertical via section addresses non-idealities inherent in the transition between vertically stacked conductive layers, a phenomenon exacerbated by technological variations. Detailed analysis and modeling of these effects have been presented in Iannacci et al. (2009), wherein it is elucidated that the transition between layers is hindered by the presence of titanium oxide films, leading to increased resistance and loss. This non-ideal behavior is aptly represented in Fig. 4, wherein a series capacitor (C_{se-v}) and resistors ($R_{se-lf-v}$ and $R_{se-hf-v}$) are incorporated to account for the reactive loss and additional series resistance induced by the oxide layer. The impact of these non-idealities on the measured S-parameters characteristics will be

covered in subsequent sections, underscoring the significance of accounting for such factors in accurate network modeling.

Transitioning to the intrinsic attenuator sub-section depicted in Fig. 5, a similar approach is adopted to model the discrete components comprising the attenuator. As with the CPW and vertical via sections, the specific details of each component utilized in the attenuator model are listed in Table 1, providing essential insights into their individual contributions to the overall network behavior.

In summary, the comprehensive modeling approach employed in delineating the CPW, vertical via, and intrinsic attenuator sections underscores the complexity and sophistication inherent in accurately capturing the behavior of RF-MEMS attenuators. By integrating insights from prior research and employing detailed modeling techniques, researchers are better equipped to understand and mitigate the impact of non-idealities, thereby enhancing the performance and reliability of RF communication systems.

Adhering to the configuration delineated in the physical device illustrated in Fig. 1, the intrinsic attenuator section is delineated into four distinct subsections within Fig. 5. Each block depicted in Fig. 5 comprises two parallel components, with one component, named $R_{se-sw-cl}$, consistent across all four subsections. This resistor serves to model the resistance encountered in the ON state of the corresponding RF-MEMS series ohmic switch, specifically when the switch is actuated and in CLOSE configuration, thereby facilitating signal conduction.

In the context of section A, $R_{se-sw-cl}$ operates in parallel with the capacitor $C_{se-sw-op}$, which characterizes the OFF state series parasitic capacitive coupling inherent in the RF-MEMS series switch when in OPEN configuration, i.e., not actuated and in its default position. The activation state of the switch dictates the electrical behavior of the subsections A_u and A_d ; for instance, when the upper branch is to be inserted, the corresponding $C_{se-sw-op}$ is deactivated, while if the upper branch is intended to remain open, the corresponding $R_{se-sw-cl}$ is deactivated.

Turning attention to sections B, C, D, featuring diverse resistive loads (R_{LB} , R_{LC} , R_{LD}), $R_{se-sw-cl}$ operates in parallel with these resistors. When the insertion of one or more resistive loads along the RF line is required, the corresponding $R_{se-sw-cl}$ components are deactivated (OPEN). Conversely, when a resistive load is intended not to affect the line, it remains active and continues to parallel the corresponding $R_{se-sw-cl}$. Notably, as the $R_{se-sw-cl}$ resistor is substantially smaller than the actual load (refer to Table 1), it effectively shorts the contribution of the load under consideration, optimizing signal transmission.

This configuration underscores the nuanced interplay between various components within the intrinsic attenuator section, facilitating precise control over signal attenuation levels and ensuring optimal performance across diverse operational scenarios.

The following section is going to cover the experimental characterization of the RF-MEMS attenuator and the comparison of the measured traces against the LEN simulated output.

4 Experiments and model analysis

This section delves into the examination of the measured S-parameters behavior of the step power attenuator incorporating RF-MEMS technology, alongside a comparative analysis of simulations versus experimental data. The discussion is organized into three subsections, each addressing distinct aspects of the analysis.

The first subsection presents the measured data of the network across various configurations, offering insights into its performance under different operational scenarios. This empirical data serves as a foundation for evaluating the efficacy of the attenuator and identifying any discrepancies between theoretical expectations and observed behavior.

In the subsequent subsection, the response of the Lumped Element Network (LEN) model depicted in Figs. 3, 4, and 5 is juxtaposed against experimental results. By comparing simulated outcomes with real-world observations, researchers can assess the accuracy and reliability of the model in capturing the intricate dynamics of the RF-

MEMS attenuator. Discrepancies or deviations between simulations and experiments may highlight areas for refinement or further investigation.

Lastly, the final subsection delves into the simulated results obtained when disregarding non-idealities associated with vertical vias, thereby assuming an idealized scenario. By isolating and examining the impact of these non-idealities, researchers can discern their influence on the overall performance of the attenuator and ascertain the extent to which they contribute to observed deviations from theoretical expectations.

Through this comprehensive analysis, researchers aim to gain a nuanced understanding of the operational behavior of the RF-MEMS attenuator, elucidating the interplay between theoretical models, simulations, and empirical measurements. Such insights are invaluable for refining design parameters, optimizing performance, and advancing the capabilities of RF communication systems.

4.1 Measured S-parameters characteristics

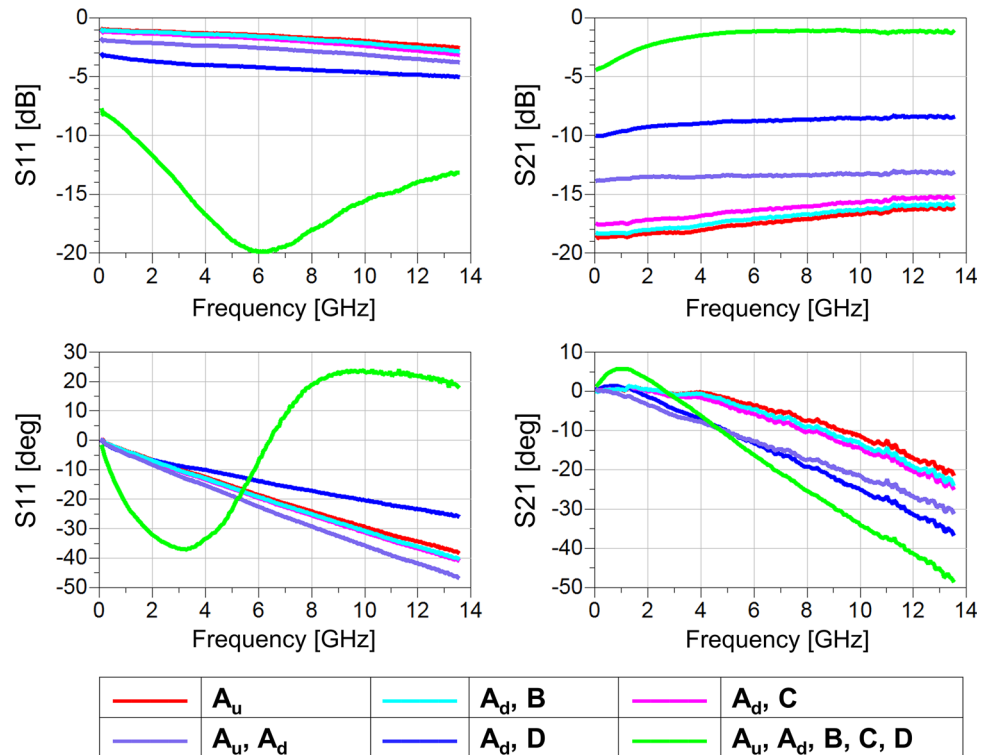
The experimental characterization of the RF-MEMS attenuator, focusing on its S-parameters, was conducted on-wafer utilizing a Vector Network Analyzer (VNA) spanning the frequency range from 100 MHz up to 13.5 GHz. The obtained data encompasses plots depicting the reflection (S11) and attenuation (S21) magnitudes, accompanied by the phase of S11 and S21. These plots are organized sequentially from the top-left to the bottom-right within Fig. 6, providing insights into the attenuator's performance across six distinct configurations.

The legend, situated at the bottom of Fig. 6, marks the activation states corresponding to each trace, thereby facilitating interpretation of the plotted data. Specifically, references to A_u and/or A_d signify the insertion of one or both branches of the attenuator. Conversely, mentions of one or more resistive sections denote the shorting of these components, indicating that their respective resistive loads are not introduced along the RF line. For instance, the designation A_d , B signifies the insertion of the sole lower branch alongside the shorting of resistor R_{LB} , while resistors R_{LC} and R_{LD} remain active, attenuating the signal.

This comprehensive experimental dataset offers valuable insights into the operational behavior of the RF-MEMS attenuator across diverse configurations, shedding light on its efficacy in facilitating precise control over signal attenuation levels and impedance matching within the RF communication system.

Directing attention to the attenuation characteristic depicted in the top-right plot, a notable attribute is the pronounced flatness observed across the entire frequency spectrum. Notably, there exists a discernible swing in attenuation levels, ranging from approximately 16–19 dB

Fig. 6 Measured S-parameters characteristics of the RF-MEMS attenuator in Fig. 1, according to different attenuation states of the network. *Top-left*, reflection (magnitude of S11 parameter); *Top-right*, attenuation (magnitude of S21 parameter); *Bottom-left*, phase of S11 parameter (reflection); *Bottom-right*, phase of S21 parameter (attenuation); *Bottom-center*, legend



when all resistive loads are inserted (A_u) to a mere 1–2 dB when these loads are shorted, and both RF branches are inserted in parallel (A_u, A_d, B, C, D). This variation underscores the attenuator’s capacity for dynamic adjustment, enabling precise control over signal attenuation levels to accommodate diverse operational requirements.

However, it is essential to acknowledge the influence of parasitic effects introduced by vertical vias, particularly attributable to the presence of capacitor C_{se-v} . These effects manifest in poorer S21 values within the low-frequency range, extending up to approximately 4 GHz. Nonetheless, as the capacitor transitions into a short, a noticeable trend towards flatness emerges, indicative of improved attenuation characteristics.

This analysis highlights the interplay between various factors influencing the attenuation behavior of the RF-MEMS attenuator, underscoring the importance of accounting for parasitic effects and component interactions in optimizing performance across different frequency regimes.

4.2 LEN model behavior accounting for vias parasitic effects

Before entering the discussion on how simulations compare to measurements, a two quantitative metrics, previously introduced in Iannacci (2023), must be recalled, as they

help in assessing the accuracy of the model in quantitative terms.

The first is labelled as Percent Magnitude Difference (PMD). Such an indicator refers to the error (in percents) between the experimental and simulated magnitude at a given frequency. The PMD for the S11 at the frequency f is expressed as follows:

$$PMD_{S11}(f) = \frac{mag(S11_M(f)) - mag(S11_S(f))}{2} * 100, \tag{1}$$

where $mag(S11_M(f))$ and $mag(S11_S(f))$ are the measured and simulated magnitude of S11 at the frequency f , respectively. Similarly, the second metric is Percent Phase Difference (PPD) is expressed as follows:

$$PPD_{S11}(f) = \frac{deg(S11_M(f)) - deg(S11_S(f))}{360} * 100, \tag{2}$$

where $deg(S11_M(f))$ and $deg(S11_S(f))$ are the measured and simulated phase of S11 at the frequency f , respectively. In the following subsections, 7 different configurations of the network are going to be discussed, referring to the LEN model accounting for via parasitic effects, also exploiting the just mentioned PMD and PPD to help elaborate quantitative considerations in the comparison of measurements and simulations.

Fig. 7 Measured S-parameters characteristics of the RF-MEMS attenuator vs. simulated response (see circuit in Figs. 3, 4, 5) when section A_u is ON. *Top-left*, reflection (magnitude of S11 parameter); *Top-right*, attenuation (magnitude of S21 parameter); *Bottom-left*, phase of S11 parameter (reflection); *Bottom-right*, phase of S21 parameter (attenuation)

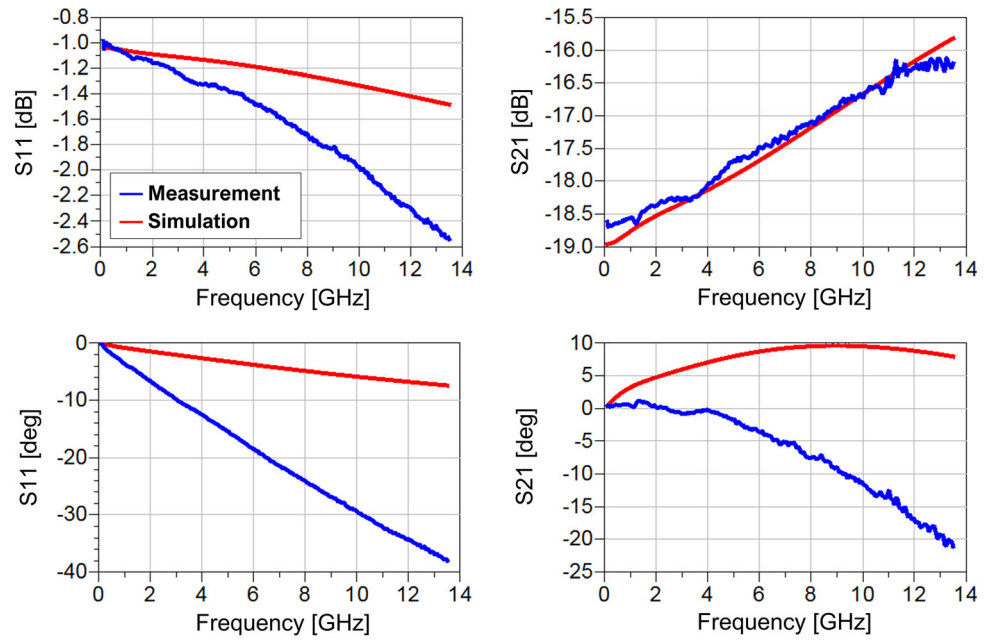
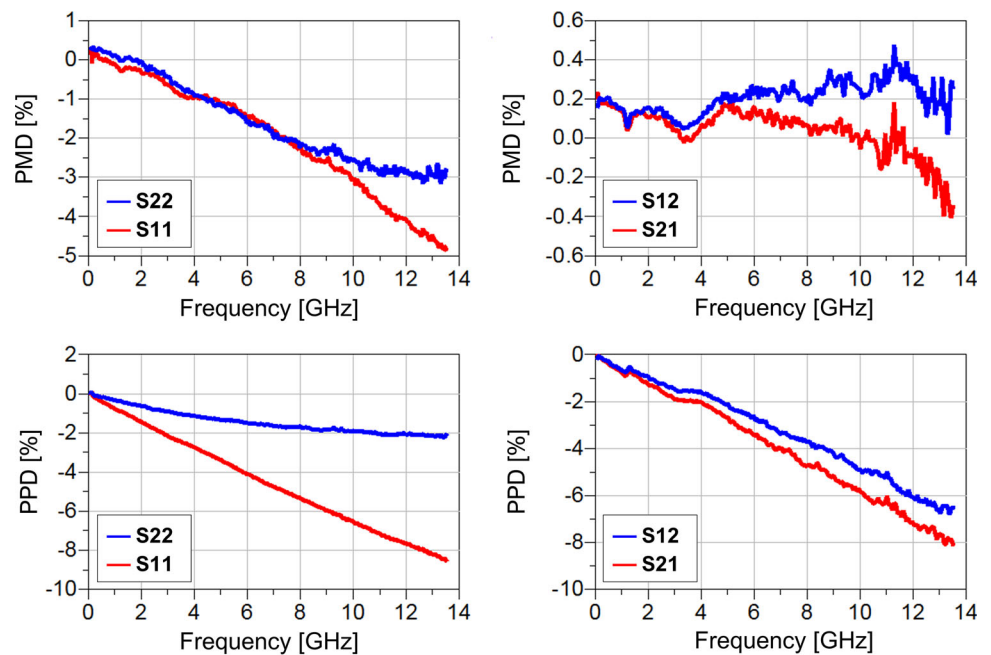


Fig. 8 Measured vs. simulated offsets related to the plots in Fig. 7 (when section A_u is ON), also including S12 and S22. *Top-left*, PMD of S11 and S22; *Top-right*, PMD of S12 and S21; *Bottom-left*, PPD of S11 and S22; *Bottom-right*, PPD of S12 and S21



4.2.1 Configuration 1—section A_u activated

The comparative analysis of the magnitude and phase of S11 and S21, derived from both experimental measurements and simulations, is showcased in Fig. 7. This comparison specifically focuses on the scenario wherein only section A_u of the RF-MEMS attenuator is activated, representing maximum attenuation. The presentation of data in Fig. 7 follows the same sequential order observed in Fig. 6, facilitating a direct comparison between experimental and simulated results across various configurations.

Through this juxtaposition, researchers aim to assess the accuracy and reliability of the simulation model in replicating the real-world behavior of the RF-MEMS attenuator under optimal attenuation conditions. Discrepancies between simulated and measured data may offer valuable insights into the efficacy of the model and highlight areas for refinement or further investigation.

Looking at the S21, an increasing disagreement of the simulated curve with respect to the experimental one is visible. However, for what concerns attenuation (S21), which is the most important parameter to be observed, the

Fig. 9 Measured S-parameters characteristics of the RF-MEMS attenuator vs. simulated response (see circuit in Figs. 3, 4, 5) when section A_u is ON, and section D is shorted. *Top-left*, reflection (magnitude of S11 parameter); *Top-right*, attenuation (magnitude of S21 parameter); *Bottom-left*, phase of S11 parameter (reflection); *Bottom-right*, phase of S21 parameter (attenuation)

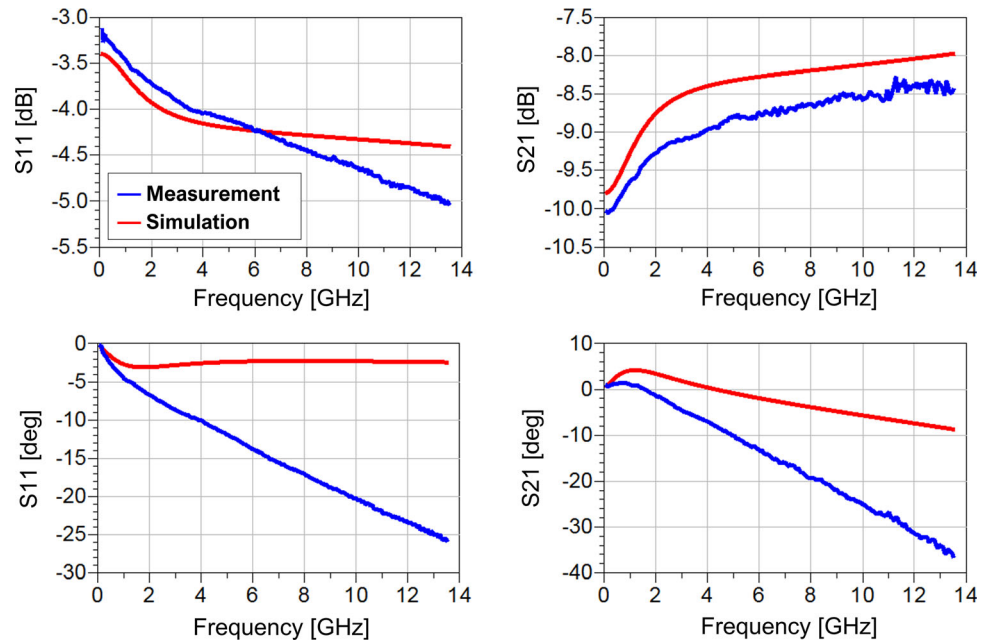
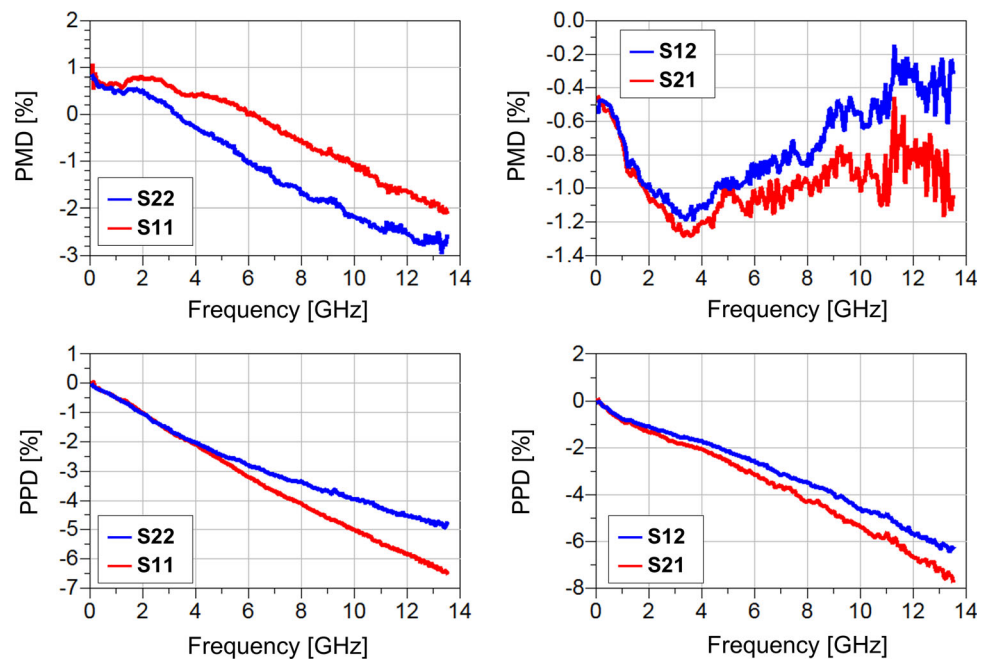


Fig. 10 Measured vs. simulated offsets related to the plots in Fig. 9 (when section A_u is ON, and section D is shorted), also including S12 and S22. *Top-left*, PMD of S11 and S22; *Top-right*, PMD of S12 and S21; *Bottom-left*, PPD of S11 and S22; *Bottom-right*, PPD of S12 and S21



accuracy of the simulation trace is rather pronounced. Looking at the phase, significant disagreement is visible both concerning reflection and attenuation. Though, the prediction of the phase is typically difficult to achieve in conjunction with good accuracy of the magnitude.

Still referring to the same RF-MEMS attenuator configuration, the plots in Fig. 8 report the PMD and PPD for the whole set of four S-parameters, i.e., reflection at port 1 and port 2 (S11 and S22, respectively), and transmission (attenuation, in this case) to port 1 and to port 2 (S12 and S12, respectively). In particular, starting from the top-left

and proceeding to the bottom-right, the plots are arranged as follows: (a) PMD of S11 and S22, (b) PMD of S12 and S21, (c) PPD of S11 and S22, (d) PPD of S12 and S21.

Looking at the PMD of reflection (to be referred to the top-left plot in Fig. 7), the error is as large as -5% in the worst case of S11. Differently, for what concerns attenuation, the prediction accuracy of the simulated model is always within $\pm 0.4\%$, for both S12 and S21, over the whole frequency range. In the case of PPD, the prediction error becomes as large as -8% .

Fig. 11 Measured S-parameters characteristics of the RF-MEMS attenuator vs. simulated response (see circuit in Figs. 3, 4, 5) when section A_d is ON, and section D is shorted. *Top-left*, reflection (magnitude of S11 parameter); *Top-right*, attenuation (magnitude of S21 parameter); *Bottom-left*, phase of S11 parameter (reflection); *Bottom-right*, phase of S21 parameter (attenuation)

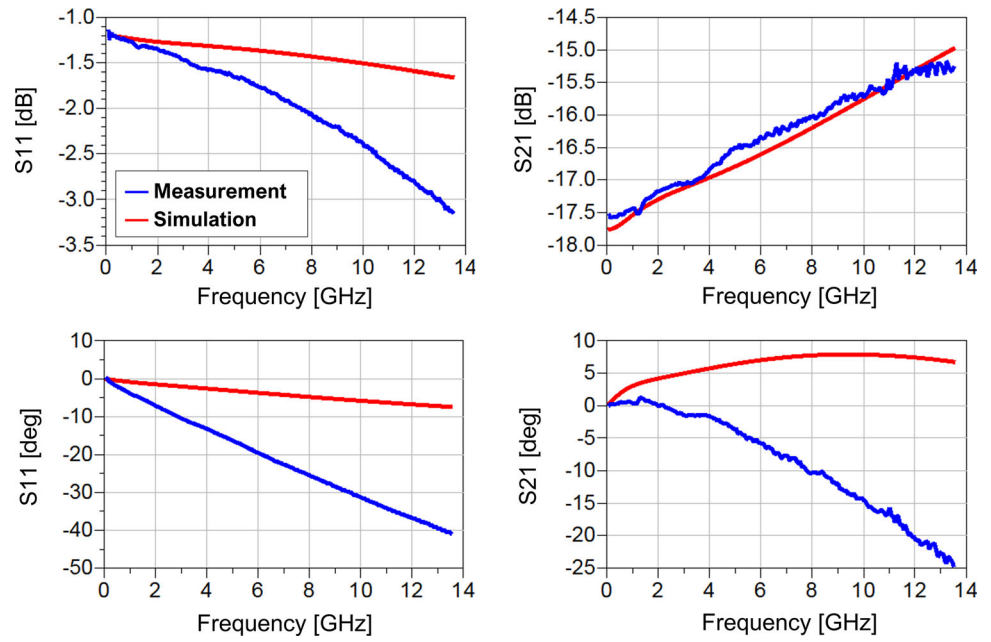
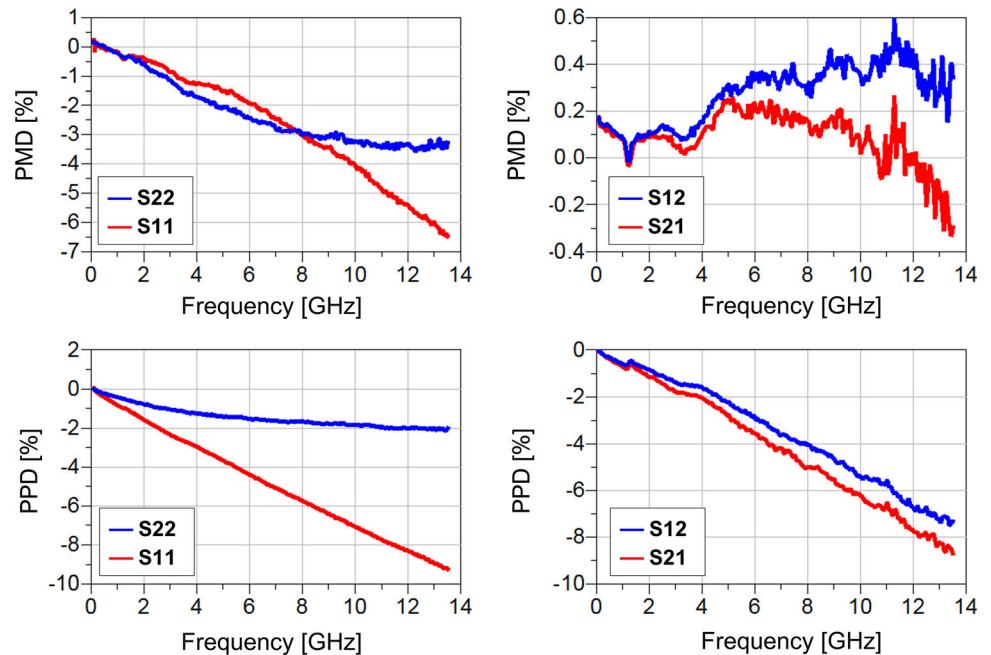


Fig. 12 Caption to be added. Measured vs. simulated offsets related to the plots in Fig. 11 (when section A_d is ON, and section D is shorted), also including S12 and S22. *Top-left*, PMD of S11 and S22; *Top-right*, PMD of S12 and S21; *Bottom-left*, PPD of S11 and S22; *Bottom-right*, PPD of S12 and S21



4.2.2 Configuration 2—section A_u activated; section D shorted

The following reported configuration is that with section A_u inserted and section D shorted. The comparison of measured and simulated S11 and S21 parameters is shown in Fig. 9, while the PMD and PPD for the complete set of S-parameters (S11, S21, S12, S22) are collected in Fig. 10.

Starting from the attenuation (top-right plot in Fig. 9), a good qualitative prediction is achieved by the simulation, while a rather constant offset is visible. This yields a PMD

(for S12 and S21) that, in the worst case, reaches -1.3% (top-right plot in Fig. 10). Concerning reflection, the superposition of the measured and simulated trace looks good up to around 6 GHz, while increasing divergence is visible above. This brings to PMD values (for S11 and S22) approaching -3% in the worst case. On the other hand, the phase disagreement for all the set of S-parameters lead to PPD values approaching -8% error, as in the previous network configuration analyzed.

Fig. 13 Measured S-parameters characteristics of the RF-MEMS attenuator vs. simulated response (see circuit in Figs. 3, 4, 5) when section A_d is ON, and section B is shorted. *Top-left*, reflection (magnitude of S11 parameter); *Top-right*, attenuation (magnitude of S21 parameter); *Bottom-left*, phase of S11 parameter (reflection); *Bottom-right*, phase of S21 parameter (attenuation)

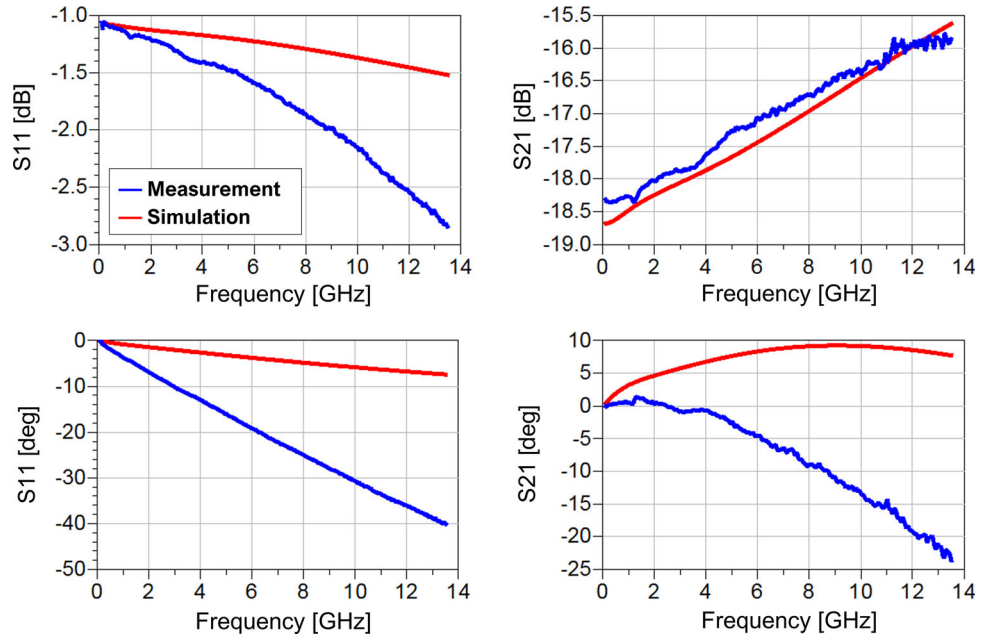
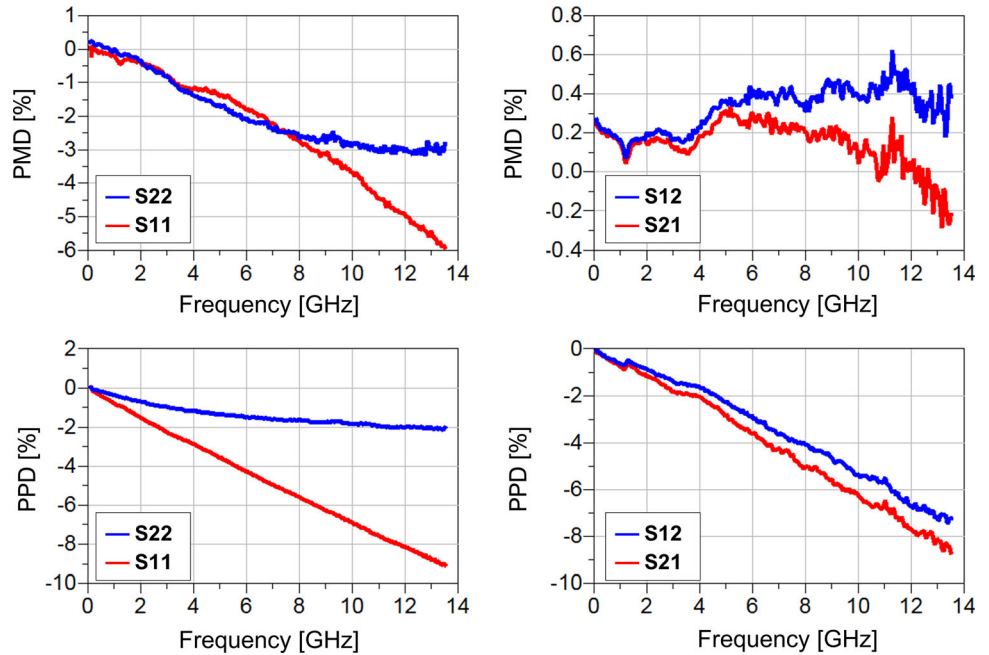


Fig. 14 Caption to be added. Measured vs. simulated offsets related to the plots in Fig. 13 (when section A_d is ON, and section B is shorted), also including S12 and S22. *Top-left*, PMD of S11 and S22; *Top-right*, PMD of S12 and S21; *Bottom-left*, PPD of S11 and S22; *Bottom-right*, PPD of S12 and S21



4.2.3 Configuration 3—section A_d activated; section C shorted

The following reported configuration is that with section A_d inserted and section C shorted. The comparison of measured and simulated S11 and S21 parameters is shown in Fig. 11, while the PMD and PPD for the complete set of S-parameters (S11, S21, S12, S22) are collected in Fig. 12.

Focusing on the attenuation (top-right plot in Fig. 11), a good match between the experimental and simulated

curves is visible. In terms of PMD (top-right plot in Fig. 12), the difference for the S21 parameter is within 0.2% up to 12 GHz, and within -0.3% up to 13.5 GHz, while the PMD of the S12 parameter is always within 0.5%. Still referring to S21 and S12, PPD is within -8% (bottom-right plot in Fig. 12). On the other hand, PMD of reflection is within -3.5% for the S22 and within -6.5% for the S11 (top-left plot in Fig. 12).

Fig. 15 Measured S-parameters characteristics of the RF-MEMS attenuator vs. simulated response (see circuit in Figs. 3, 4, 5) when sections A_u and A_d are ON. *Top-left*, reflection (magnitude of S11 parameter); *Top-right*, attenuation (magnitude of S21 parameter); *Bottom-left*, phase of S11 parameter (reflection); *Bottom-right*, phase of S21 parameter (attenuation)

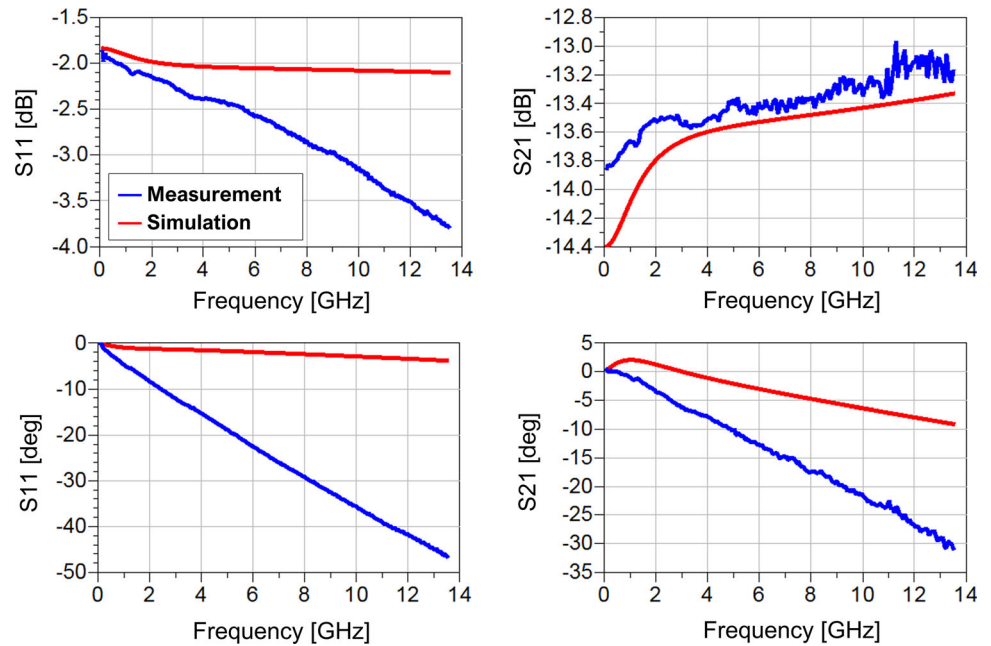
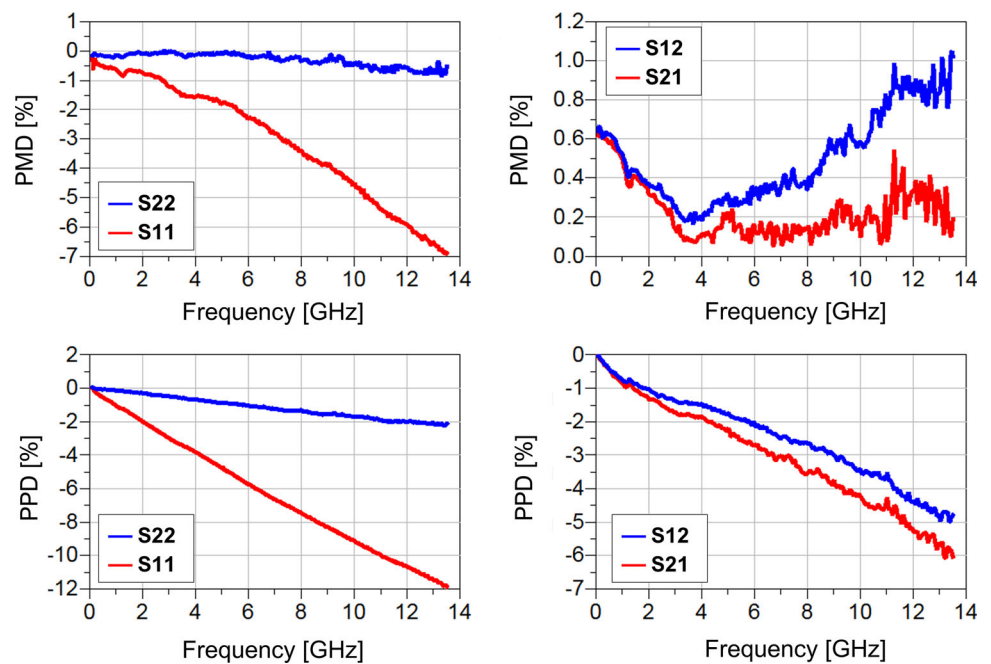


Fig. 16 Measured vs. simulated offsets related to the plots in Fig. 15 (when sections A_u and A_d are ON), also including S12 and S22. *Top-left*, PMD of S11 and S22; *Top-right*, PMD of S12 and S21; *Bottom-left*, PPD of S11 and S22; *Bottom-right*, PPD of S12 and S21



4.2.4 Configuration 4—section A_d activated; section B shorted

The following reported configuration is that with section A_d inserted and section B shorted. The comparison of measured and simulated S11 and S21 parameters is shown in Fig. 13, while the PMD and PPD for the complete set of S-parameters (S11, S21, S12, S22) are collected in Fig. 14.

Starting as before from looking at the attenuation (top-right plot in Fig. 13), a good match between the simulated and measured curves is visible. This brings to PMD better

than 0.5% for S12, and within $\pm 0.3\%$ for S12 (top-right plot in Fig. 14). The corresponding PPD is within -7 and -9% , for S12 and S21, respectively (bottom-right plot in Fig. 14). On the other hand, the PMD and PPD of reflection (S22) is within -3 and -2% , respectively, as visible in the top-left and bottom-left plots in Fig. 14.

4.2.5 Configuration 5—sections A_u and A_d activated

The following reported configuration is that with section A_u and A_d inserted (in parallel). The comparison of

Fig. 17 Measured S-parameters characteristics of the RF-MEMS attenuator vs. simulated response (see circuit in Figs. 3, 4, 5) when sections A_u and A_d are ON, and sections B, C and D are shorted. *Top-left*, reflection (magnitude of S11 parameter); *Top-right*, attenuation (magnitude of S21 parameter); *Bottom-left*, phase of S11 parameter (reflection); *Bottom-right*, phase of S21 parameter (attenuation)

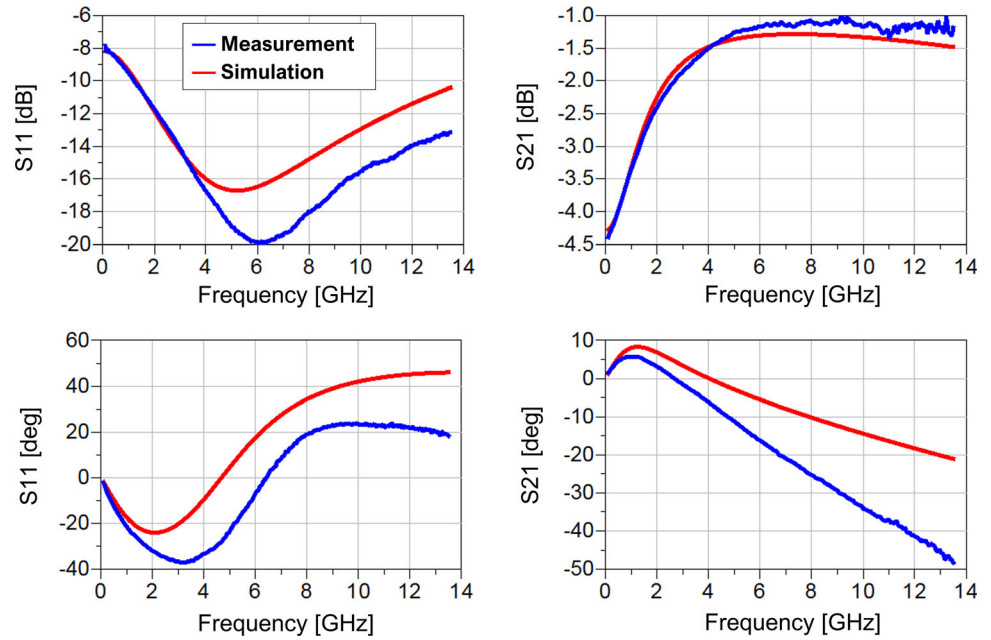
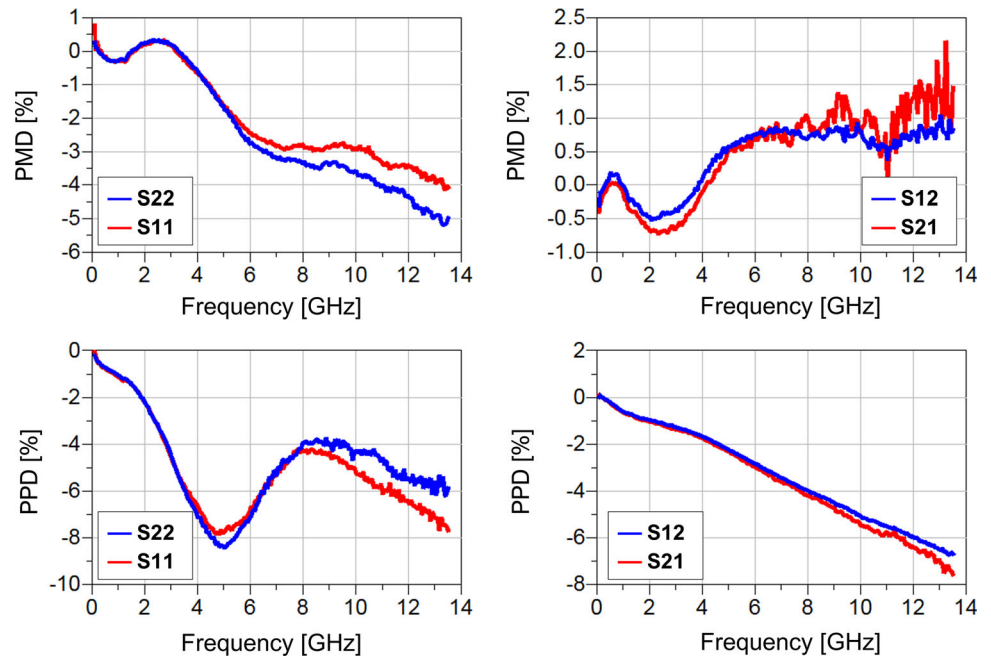


Fig. 18 Measured vs. simulated offsets related to the plots in Fig. 7 (when sections A_u and A_d are ON, and sections B, C and D are shorted), also including S12 and S22. *Top-left*, PMD of S11 and S22; *Top-right*, PMD of S12 and S21; *Bottom-left*, PPD of S11 and S22; *Bottom-right*, PPD of S12 and S21



measured and simulated S11 and S21 parameters is shown in Fig. 15, while the PMD and PPD for the complete set of S-parameters (S11, S21, S12, S22) are collected in Fig. 16.

Focusing at first on attenuation, a good qualitative and quantitative match is visible in the top-right plot in Fig. 15. This configuration is the first to be observed with both branches connected in parallel. This leads to a reduction in the cumulative resistive load, which makes the non-idealities of vertical vias emerge more visible in the lower portion of the frequency range. In terms of PMD, the error is within 0.9% for S12, and within 0.6% for S21 (top-right

plot in Fig. 16). In particular, in the latter case, the PMD within 0.3% from 4 GHz up to 13.5 GHz. The PPD of attenuation is within -8% in the worst case, which is that of S21, as reported in the bottom-right plot in Fig. 16. Looking at reflection, the case of S22 shows a very-good match, as PMD and PPD are within -1 and -2%, respectively (see top-left and bottom-left plots in Fig. 16). Diversely, the same indicators for the S11 are within -7 and -12%, respectively.

Fig. 19 Measured S-parameters characteristics of the RF-MEMS attenuator vs. simulated response (see circuit in Figs. 3, 4, 5) when section A_u is ON, and sections B, C and D are shorted. *Top-left*, reflection (magnitude of S11 parameter); *Top-right*, attenuation (magnitude of S21 parameter); *Bottom-left*, phase of S11 parameter (reflection); *Bottom-right*, phase of S21 parameter (attenuation)

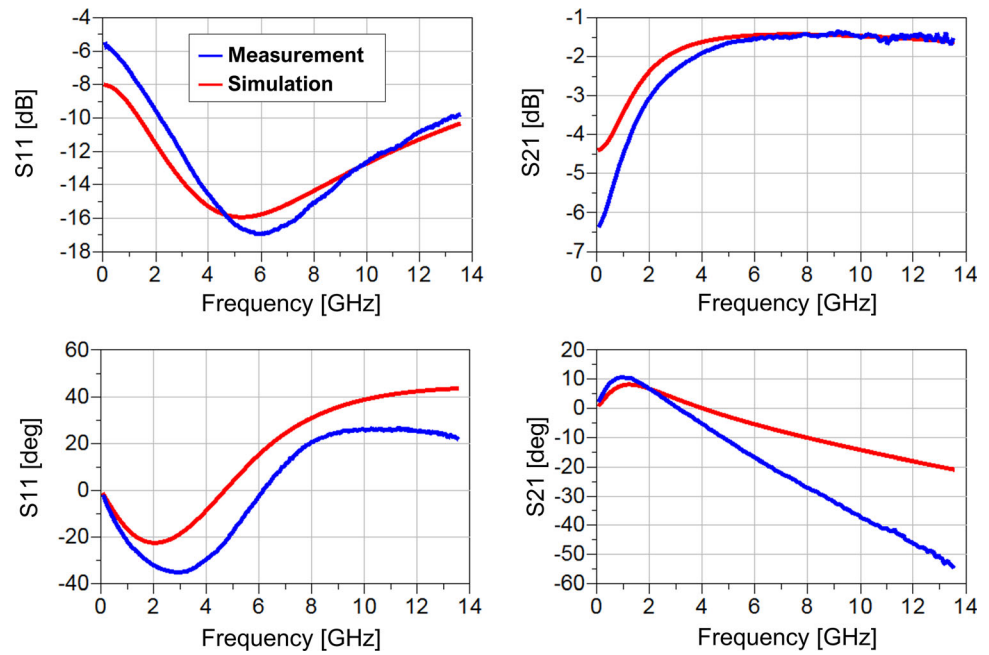
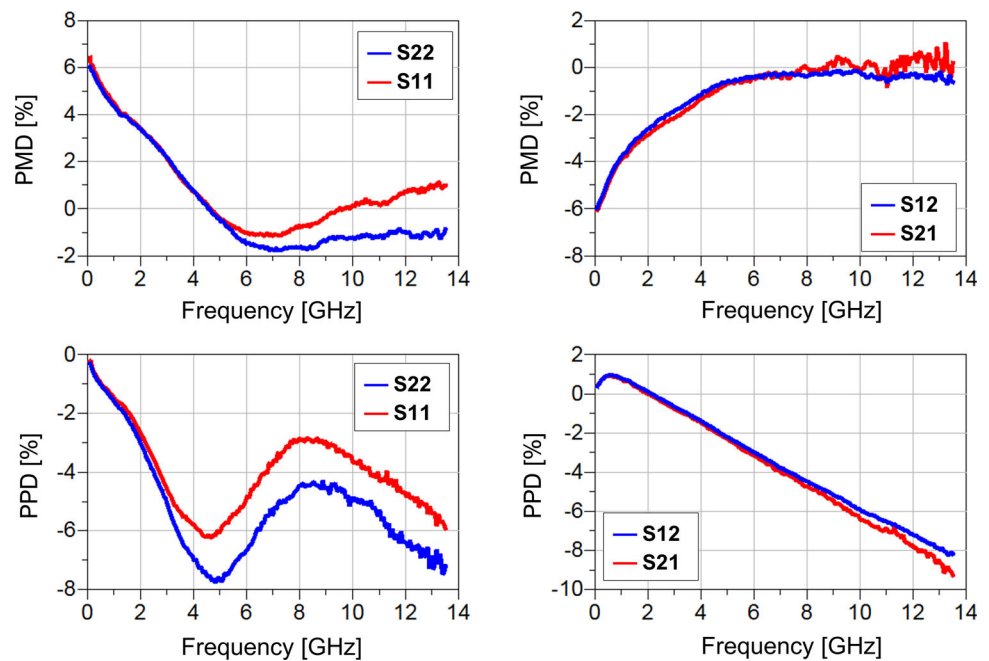


Fig. 20 Measured vs. simulated offsets related to the plots in Fig. 19 (when section A_u is ON, and sections B, C and D are shorted), also including S12 and S22. *Top-left*, PMD of S11 and S22; *Top-right*, PMD of S12 and S21; *Bottom-left*, PPD of S11 and S22; *Bottom-right*, PPD of S12 and S21



4.2.6 Configuration 6—sections A_u and A_d activated; sections B, C and D shorted

The following reported configuration is that with section A_u and A_d inserted (in parallel), and sections B, C and D shorted. The comparison of measured and simulated S11 and S21 parameters is shown in Fig. 17, while the PMD and PPD for the complete set of S-parameters (S11, S21, S12, S22) are collected in Fig. 18.

This configuration is the most interesting to see in order to understand the effectiveness of the modelling approach targeted to the technological non-idealities of vertical vias. In fact, in this particular case, all the loading resistors are shorted. Therefore, the signal attenuation is at its minimum, and the vias parasitic effects, in turn, are most visible. Starting from the attenuation parameter, shown in the top-right plot in Fig. 17, the influence of non-ideal vias is very-large in the low-portion of the analyzed frequency range, up to around 4 GHz. Such behavioral feature is

predicted rather accurately by the simulated trace, leading to PMD for S12 ranging between -0.5 and 0.7% (top-right plot in Fig. 18). Also relevantly, the phase characteristic of the attenuation parameter is qualitatively predicted rather well by the model, as visible in the bottom-right plot in Fig. 17, corresponding to PPD within -7% (bottom-right plot in Fig. 18). Focusing now on reflection, a good qualitative match between experiments and simulations is also visible, both concerning magnitude and phase (top-left and bottom-left plots in Fig. 17, respectively). This yields PMD within -5% (top-left plot in Fig. 18) and PPD within -8% (bottom-left plot in Fig. 18).

4.2.7 Configuration 7—section A_u activated; sections B, C and D shorted

The following reported configuration is that with section A_u inserted and sections B, C and D shorted. The comparison of measured and simulated S11 and S21 parameters is shown in Fig. 19, while the PMD and PPD for the complete set of S-parameters (S11, S21, S12, S22) are collected in Fig. 20.

As in the previous configuration, also in the current case the resistive load contribution is minimal, and the effects of non-idealities more visible. With reference to attenuation, once again the influence on the S21 parameter is large and visible up to around 4–5 GHz. Similarly, the qualitative and quantitative prediction of the simulated trace is rather satisfactory, both for the magnitude and phase of the S21 (top-right and bottom-right plots in Fig. 19, respectively). In particular, a certain disagreement is visible between the measured and simulated S21 in the lower frequency range.

This brings to PMD starting from -6%, then reducing to around -0.5% at about 5 GHz, to remain to such a limited extent in the rest of the spectrum (top-right plot in Fig. 20). Concerning the PPD in the bottom-right plot in Fig. 20, it is within -9%. Stepping now to analyzing the reflection behavior (S11), a good qualitative match is visible in the top-left and bottom-left plots in Fig. 19, with reference to the magnitude and phase of the S11, respectively. In particular, focusing on the magnitude of reflection, a mismatch more pronounced in the low frequency range is visible, similarly to what discussed above for attenuation. This brings to PMD that starts from 6%, and then decreases to about -1.5% (S22) and ± 1% (top-left plot in Fig. 20). Finally, the PPD of reflection is within -6% (S11) and -8% (S22), as reported in the bottom-left plot in Fig. 20.

4.3 LEN model behavior in the ideal case

The scope of this last section is to develop some insight into the behavior of an ideal LEN model, i.e., without accounting for the unwanted parasitic effects of vertical vias transitions, previously discussed in this work. To do so, in the schematic close-up in Fig. 4, the three elements related to the vertical vias section are simply deactivated and shorted. Therefore, simulations are performed with reference to the two network configurations previously discussed in Sect. 4.2.

4.3.1 Configuration 1—section A_u activated

The reflection (S11) and attenuation (S21) when the A_u section is ON, are shown in Fig. 21.

Fig. 21 Measured S-parameters characteristics of the RF-MEMS attenuator vs. simulated response (see circuit in Figs. 3, 4, 5) without modelling vertical vias parasitic effects (ideal case), when section A_u is ON. *Top-left*, reflection (magnitude of S11 parameter); *Top-right*, attenuation (magnitude of S21 parameter); *Bottom-left*, phase of S11 parameter (reflection); *Bottom-right*, phase of S21 parameter (attenuation)

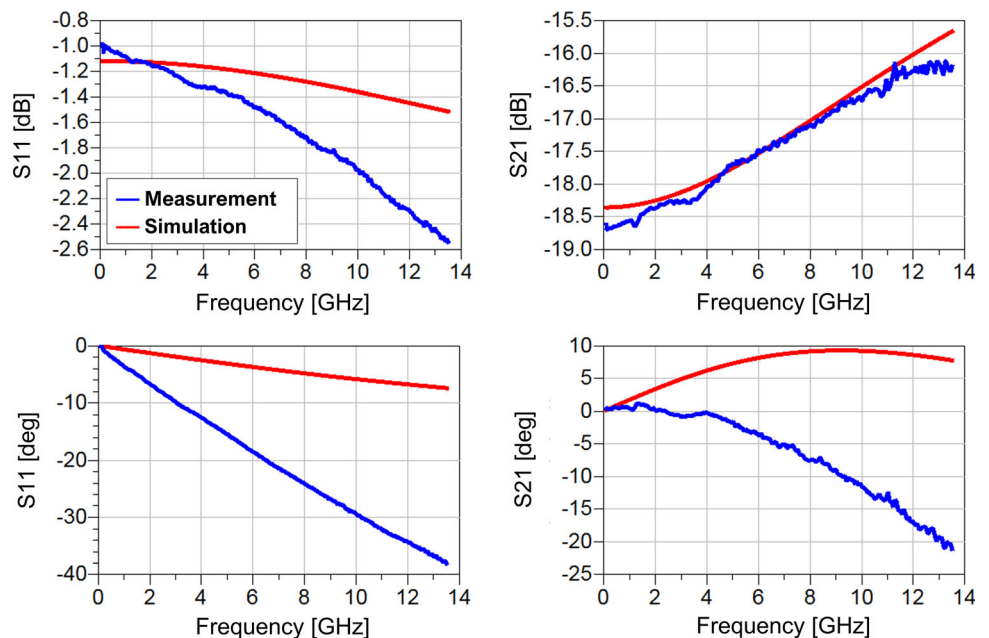


Fig. 22 Measured vs. simulated offsets related to the plots in Fig. 21 (when section A_u is ON), also including S12 and S22. *Top-left*, PMD of S11 and S22; *Top-right*, PMD of S12 and S21; *Bottom-left*, PPD of S11 and S22; *Bottom-right*, PPD of S12 and S21

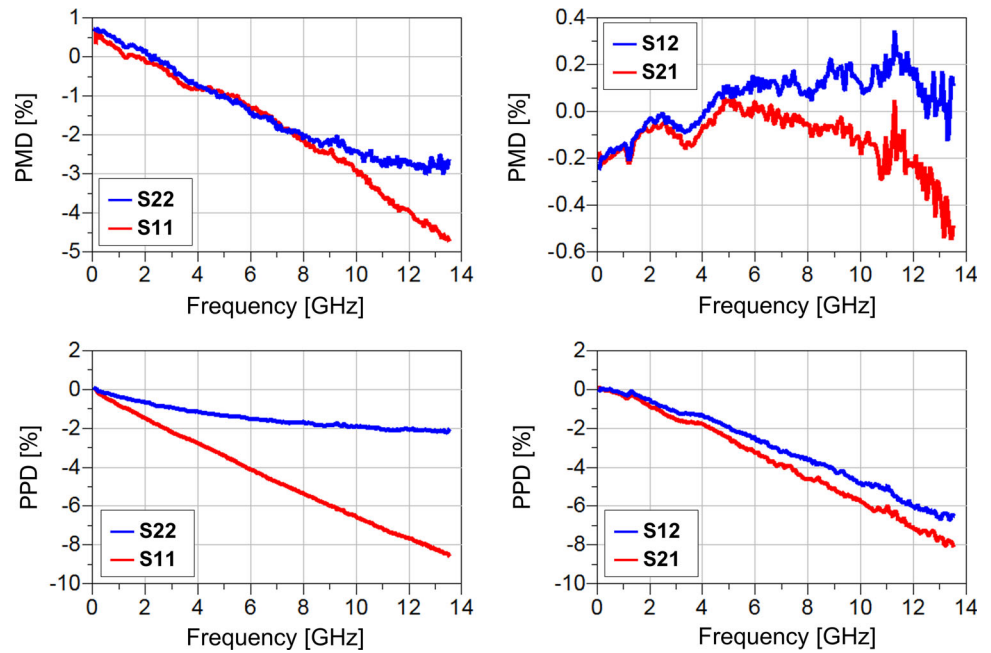
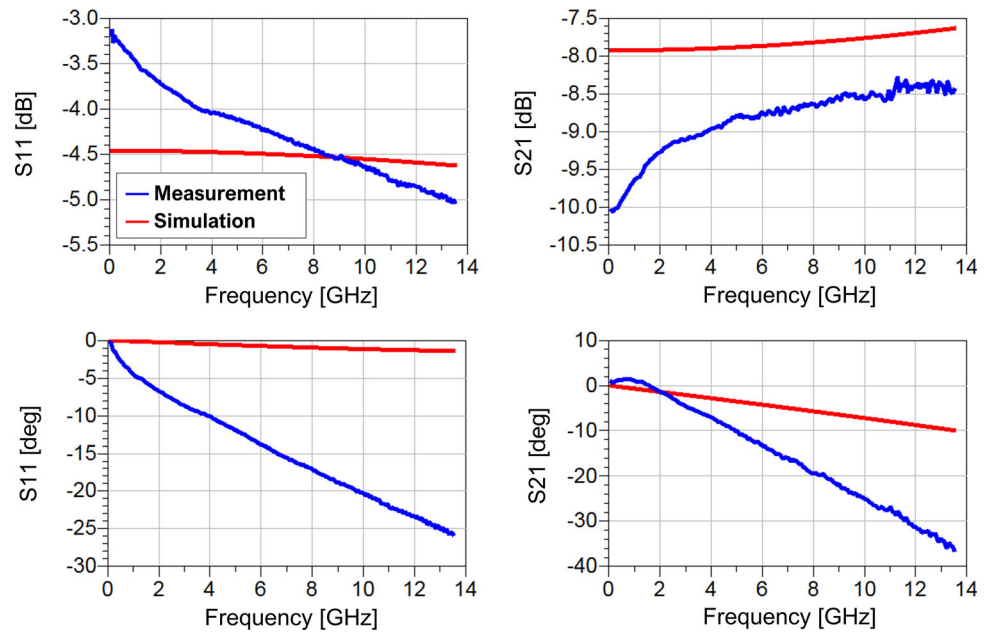


Fig. 23 Measured S-parameters characteristics of the RF-MEMS attenuator vs. simulated response (see circuit in Figs. 3, 4, 5) without modelling vertical vias parasitic effects (ideal case), when section A_u is ON, and section D is shorted. *Top-left*, reflection (magnitude of S11 parameter); *Top-right*, attenuation (magnitude of S21 parameter); *Bottom-left*, phase of S11 parameter (reflection); *Bottom-right*, phase of S21 parameter (attenuation)



Looking at the attenuation (S21) plot, the qualitative behavior of the simulated trace seems less accurate than in the previous case reported in Fig. 7 (top-right plot). This yield PMD values of S12 and S21 that approach, in the worst case, -0.6% error (see top-right plot in Fig. 22), i.e., slightly worse than in the real case with vertical vias parasitic effects, shown in Fig. 8. On the other hand, the characteristics and error of reflection, along with the phases of all the parameters, are in line with what discussed before in Figs. 7 and 8.

4.3.2 Configuration 2—section A_u activated; section D shorted

The context changes quite significantly when looking at the configuration in which section A_u is ON and section D is shorted. The results related to the S-parameters and PMD/PPD in the ideal case (no vias parasitic effects) are reported in Figs. 23 and 24, respectively, and they must be compared to previous Figs. 9 and 10 (vias parasitic effects modelled).

Fig. 24 Measured vs. simulated offsets related to the plots in Fig. 23 (when section A_u is ON, and section D is shorted), also including S12 and S22. *Top-left*, PMD of S11 and S22; *Top-right*, PMD of S12 and S21; *Bottom-left*, PPD of S11 and S22; *Bottom-right*, PPD of S12 and S21

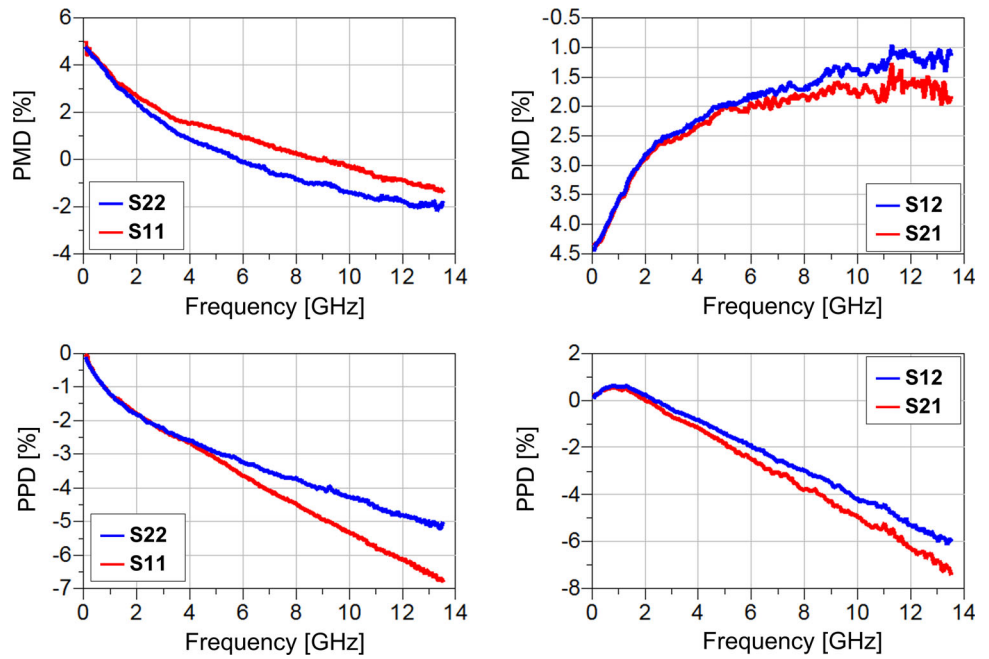
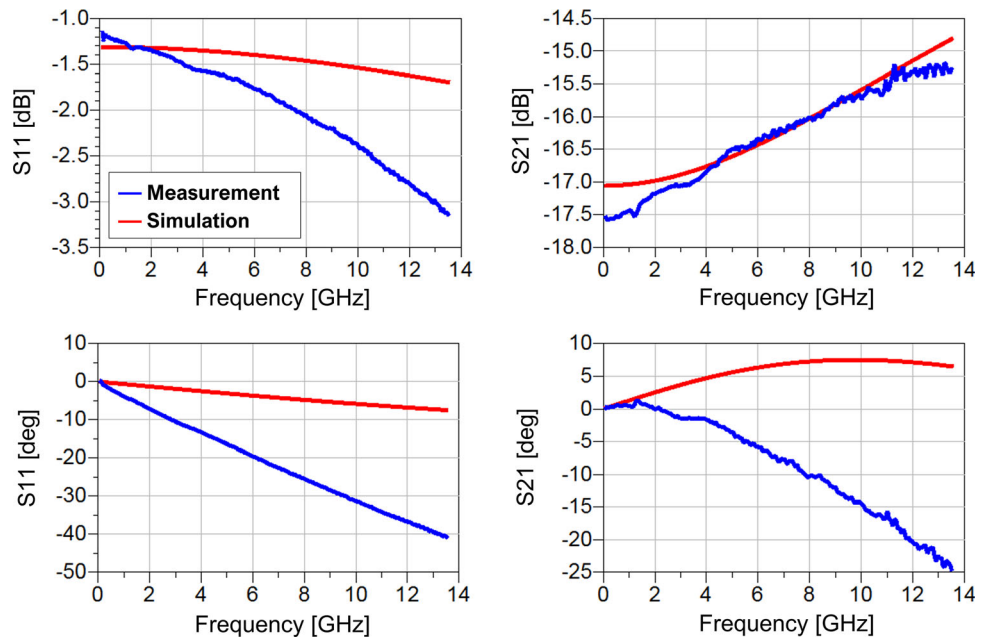


Fig. 25 Measured S-parameters characteristics of the RF-MEMS attenuator vs. simulated response (see circuit in Figs. 3, 4, 5) without modelling vertical vias parasitic effects (ideal case), when section A_d is ON, and section C is shorted. *Top-left*, reflection (magnitude of S11 parameter); *Top-right*, attenuation (magnitude of S21 parameter); *Bottom-left*, phase of S11 parameter (reflection); *Bottom-right*, phase of S21 parameter (attenuation)



Looking at the attenuation parameter in the top-right plot in Fig. 23, the disagreement of the simulated trace with respect to experiments is evident, both in qualitative and quantitative terms, especially in the lower portion of the frequency range. This yields PMD error for S12 and S21 that starts from the worst value of 4.5%, and then decreases to the 1–2% range for the two curves, at 13.5 GHz (see top-right plot in Fig. 24). This context is quite different with respect to the 0.4–0.6% maximum error reported in the case of the LEN that also models the parasitic effects of vias.

This is because the unwanted behavior of vias is dominated by the series capacitance of the residual thin titanium oxide. This affects mainly the RF characteristics in the lower frequency range, as it is also evident when looking at reflection (top-left plot in Fig. 23) and at the corresponding PMD (top-left plot in Fig. 24). Also importantly, this effects is less visible in the previous case reported in Figs. 21 and 22, as the maximum resistive load allowed by the network is involved. Given the resulting large attenuation level, the effect of the parasitic series

Fig. 26 Measured vs. simulated offsets related to the plots in Fig. 25 (when section A_d is ON, and section C is shorted), also including S12 and S22. *Top-left*, PMD of S11 and S22; *Top-right*, PMD of S12 and S21; *Bottom-left*, PPD of S11 and S22; *Bottom-right*, PPD of S12 and S21

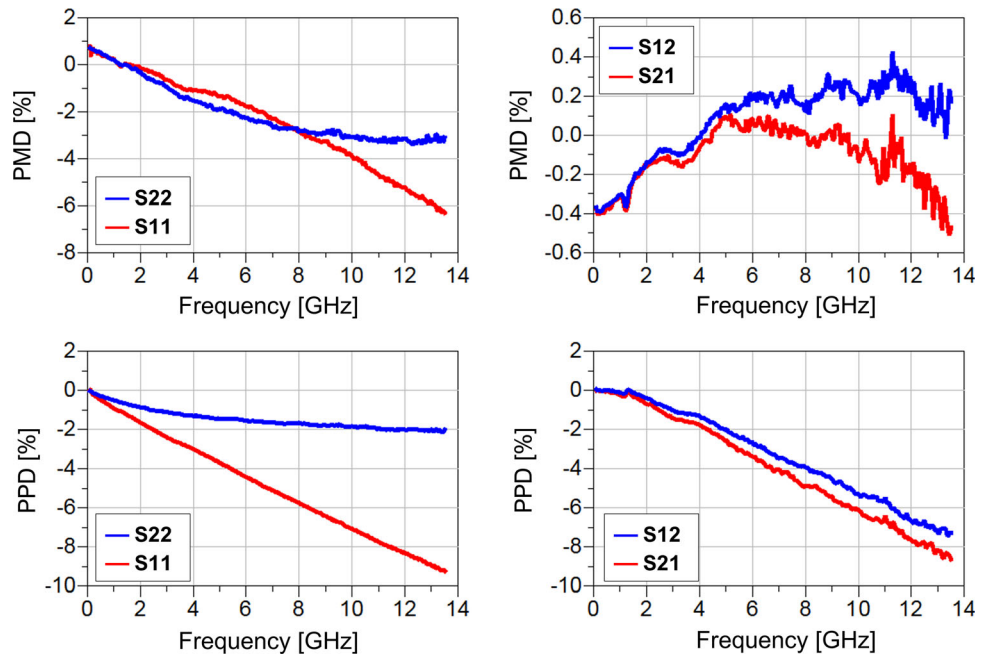
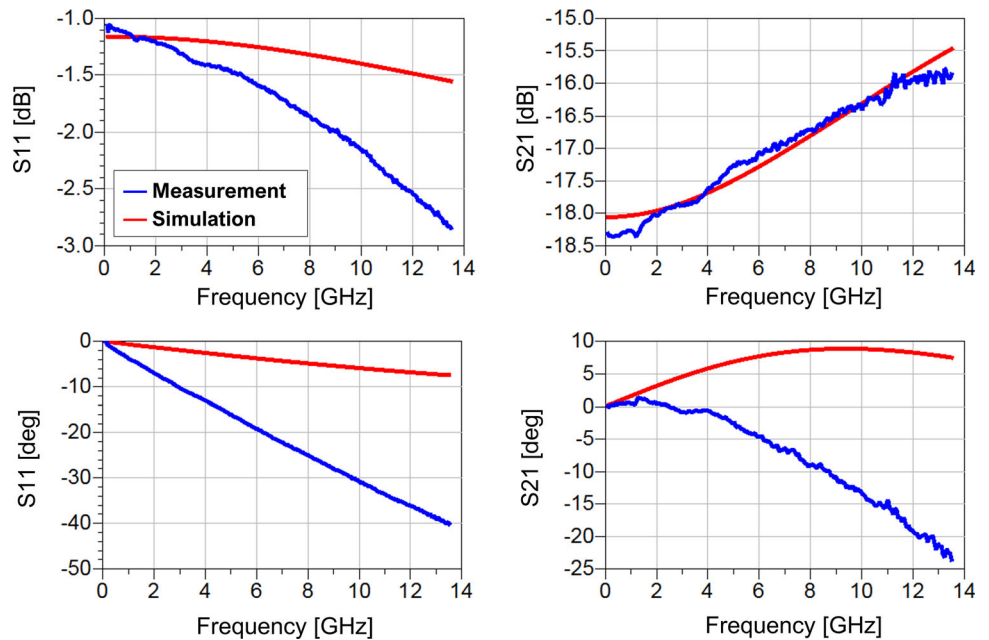


Fig. 27 Measured S-parameters characteristics of the RF-MEMS attenuator vs. simulated response (see circuit in Figs. 3, 4, 5) without modelling vertical vias parasitic effects (ideal case), when section A_d is ON, and section B is shorted. *Top-left*, reflection (magnitude of S11 parameter); *Top-right*, attenuation (magnitude of S21 parameter); *Bottom-left*, phase of S11 parameter (reflection); *Bottom-right*, phase of S21 parameter (attenuation)



capacitor is somehow “shadowed” in the S-parameters plots.

Finally, the phase of S-parameters and the corresponding PPD traces show values comparable to all the previous cases reported in this work.

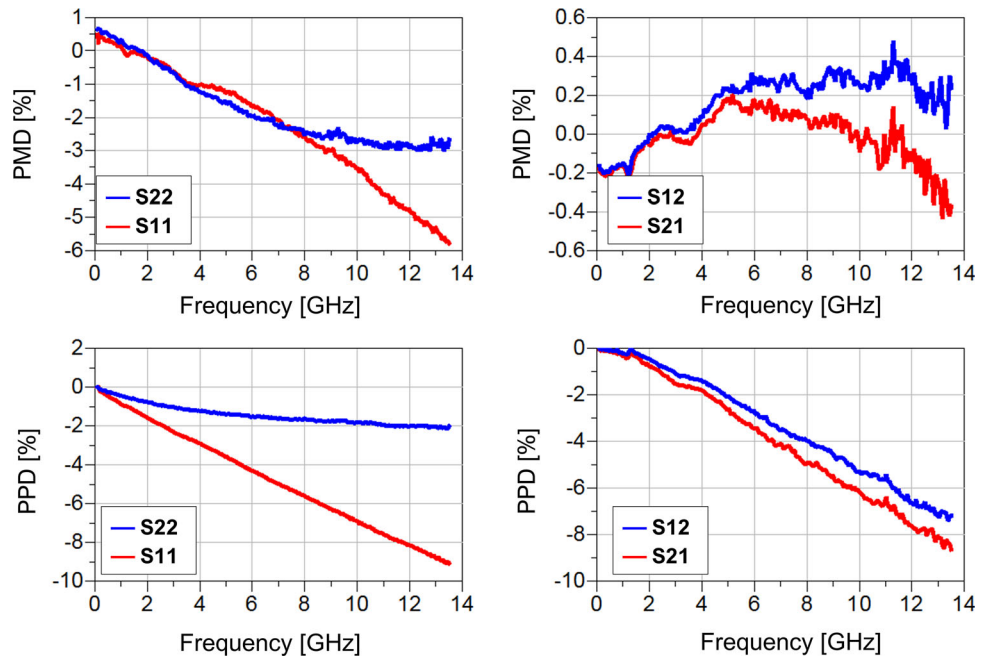
4.3.3 Configuration 3—section A_d activated; section C shorted

This configuration features one single branch activated (i.e., section A_d) and the intermediate resistive load shorted

(i.e., section C). This said, the simulated attenuation without accounting for vias parasitic effect (top-right plot in Fig. 25), must be compared to that related to the model that accounts for such non-idealities (top-right plot in Fig. 11). In the former case, larger disagreement with respect to experiments is visible in the lower part of the frequency range. Moreover, the nearly-linear behavior in the rest of the spectrum is slightly more misaligned with respect to the case reported in Fig. 11.

In terms of PMD for the attenuation parameter, the value for S12 is within 0.4% in the case of vias effects included

Fig. 28 Measured vs. simulated offsets related to the plots in Fig. 27 (when section A_d is ON, and section B is shorted), also including S12 and S22. *Top-left*, PMD of S11 and S22; *Top-right*, PMD of S12 and S21; *Bottom-left*, PPD of S11 and S22; *Bottom-right*, PPD of S12 and S21



(top-right plot in Fig. 12), while it ranges between -0.4 and 0.3% when vias are neglected (top-right plot in Fig. 26). Concerning S21, the PMD is within -0.3 and 0.2% in the case of vias effects included (top-right plot in Fig. 12), while it ranges between -0.5 and 0.1% when vias are neglected (top-right plot in Fig. 26).

The other parameters, i.e., reflection magnitude and the phase of attenuation and reflection, exhibit comparable behavior in the case of vias modelling included and not included. To this end, see all the plots in Figs. 11 and 12, to be confronted to those in Figs. 25 and 26.

4.3.4 Configuration 4—section A_d activated; section B shorted

This configuration features one single branch activated (i.e., section A_d) and the intermediate resistive load shorted (i.e., section B). Reasoning around the attenuation, the top-right plot in Fig. 27 (LEN without vias parasitic effects) should be compared to the top-right plot in Fig. 13 (LEN with vias parasitic effects included). For the qualitative point of view, the results in Fig. 13 are more accurate than in Fig. 27.

Fig. 29 Measured S-parameters characteristics of the RF-MEMS attenuator vs. simulated response (see circuit in Figs. 3, 4, 5) without modelling vertical vias parasitic effects (ideal case), when sections A_u and A_d are ON. *Top-left*, reflection (magnitude of S11 parameter); *Top-right*, attenuation (magnitude of S21 parameter); *Bottom-left*, phase of S11 parameter (reflection); *Bottom-right*, phase of S21 parameter (attenuation)

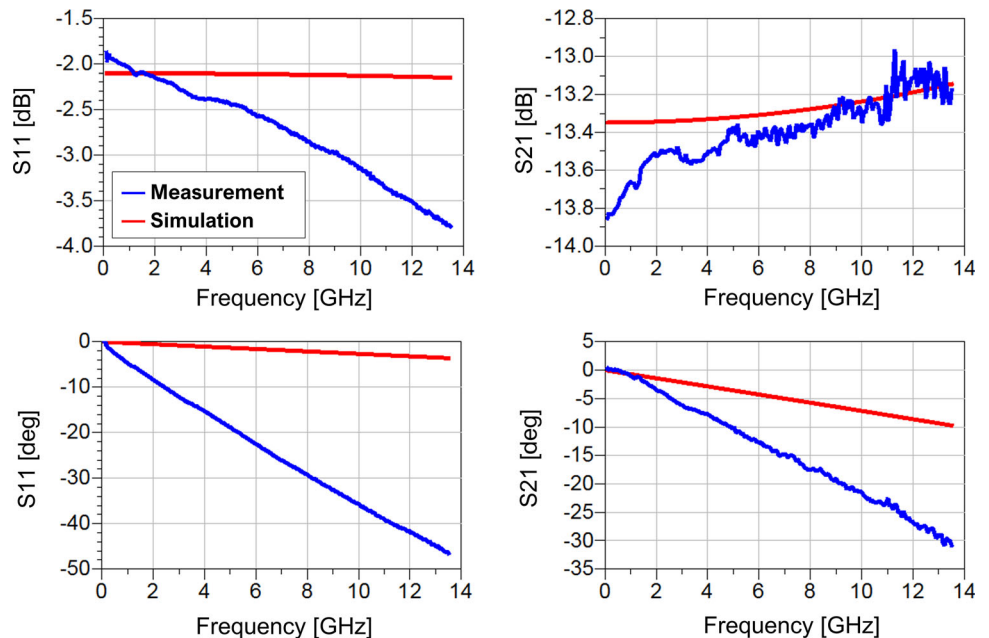
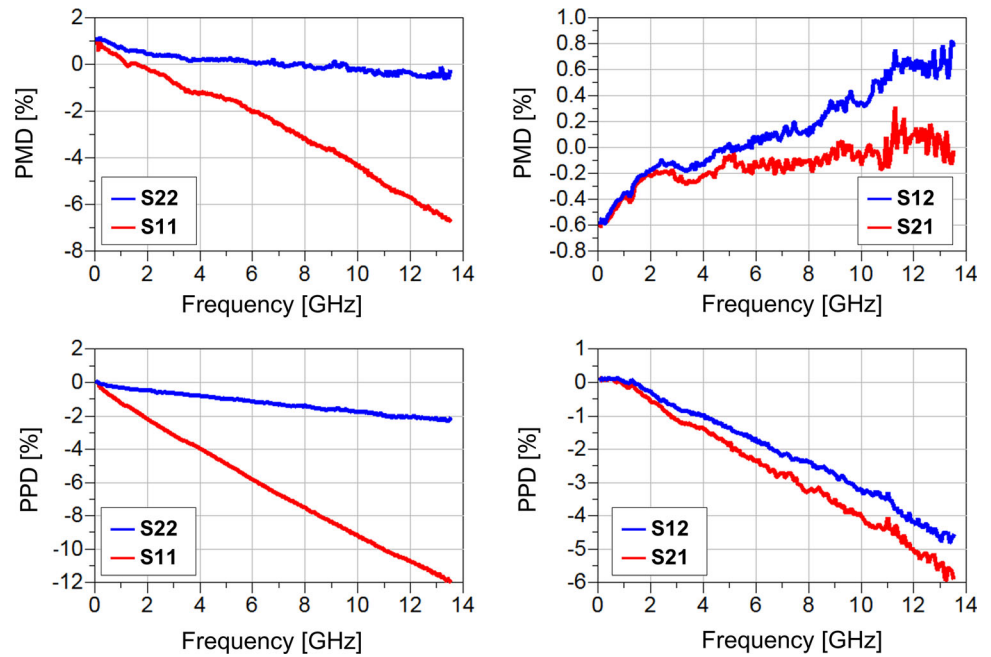


Fig. 30 Measured vs. simulated offsets related to the plots in Fig. 29 (when sections A_u and A_d are ON), also including S12 and S22. *Top-left*, PMD of S11 and S22; *Top-right*, PMD of S12 and S21; *Bottom-left*, PPD of S11 and S22; *Bottom-right*, PPD of S12 and S21



For what concerns the corresponding PMD, the error is comparable in the two cases, with just small differences. To this end, refer to the top-right plot in Fig. 28 and the one in Fig. 14. Similar considerations apply to the other parameters, i.e., reflection, phase of attenuation and reflection, as well as the corresponding PMD and PPD. Further considerations related to the comparison of all the subplots in Figs. 13 and 14, in relation to those in Figs. 27 and 28, are left to the reader.

4.3.5 Configuration 5—sections A_u and A_d activated

In this configuration, all the resistive loads are included on the RF line. At the same time, sections A_u and A_d are activated. This means that the current configuration is the one with the smaller attenuation load observed to this point. Recalling previous considerations on the impact of vertical vias non-idealities on the S-parameters, in relation to the resistive load extent on the RF line, a larger difference is expected between the LEN with modelled vias and the other one without. To this end, starting as always from

Fig. 31 Measured S-parameters characteristics of the RF-MEMS attenuator vs. simulated response (see circuit in Figs. 3, 4, 5) without modelling vertical vias parasitic effects (ideal case), when sections A_u and A_d are ON, and sections B, C and D are shorted. *Top-left*, reflection (magnitude of S11 parameter); *Top-right*, attenuation (magnitude of S21 parameter); *Bottom-left*, phase of S11 parameter (reflection); *Bottom-right*, phase of S21 parameter (attenuation)

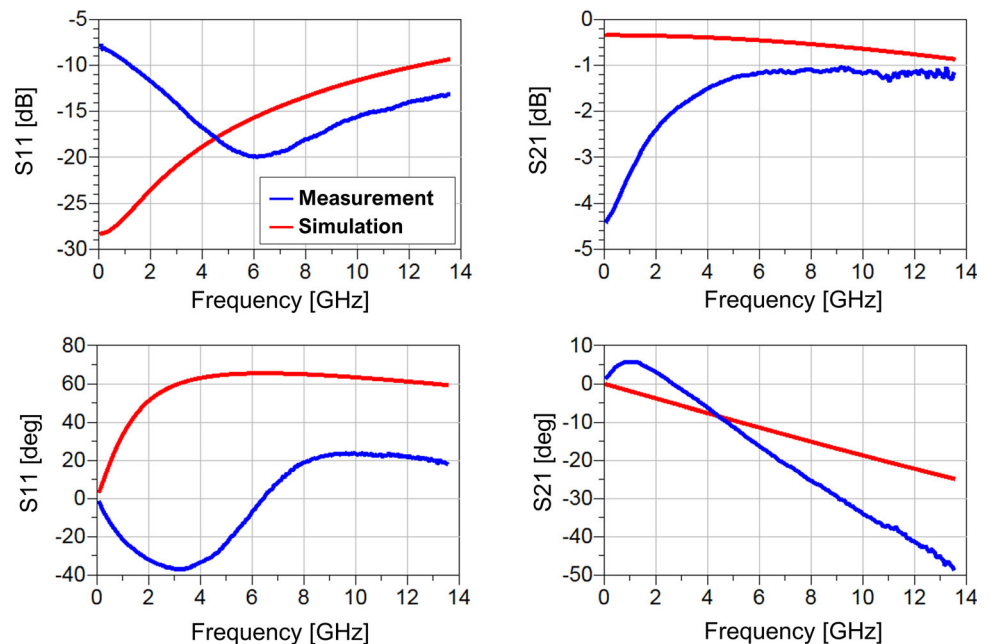
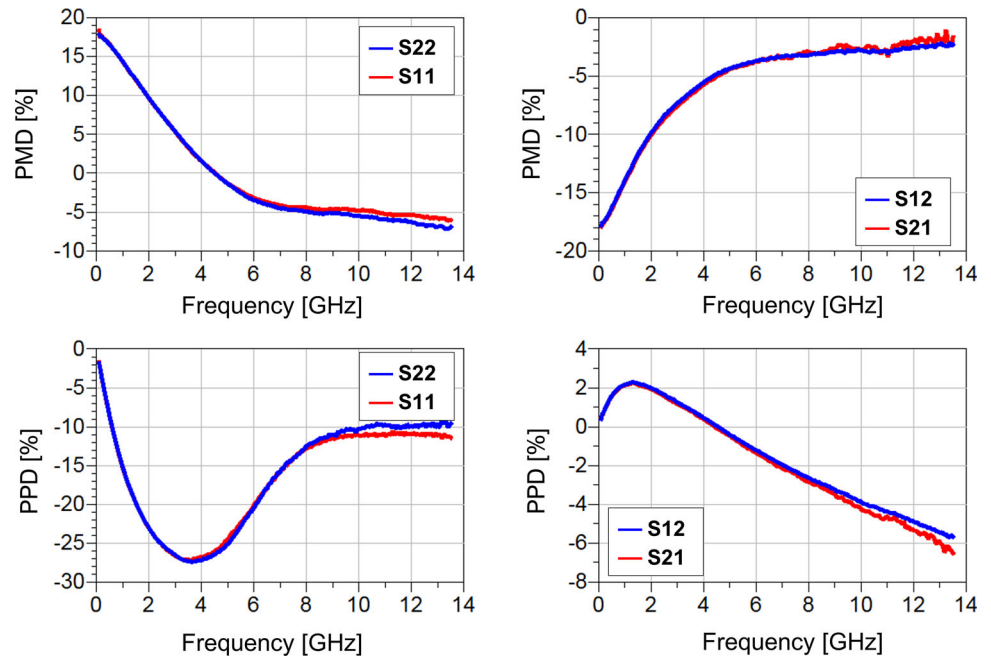


Fig. 32 Measured vs. simulated offsets related to the plots in Fig. 31 (when sections A_u and A_d are ON, and sections B, C and D are shorted), also including S12 and S22. *Top-left*, PMD of S11 and S22; *Top-right*, PMD of S12 and S21; *Bottom-left*, PPD of S11 and S22; *Bottom-right*, PPD of S12 and S21



the attenuation, it is worth comparing the top-right plot in Fig. 15 (vias parasitic effects included) with the top-right plot in Fig. 29 (via parasitic effects neglected—ideal case). It is evident that from the qualitative point of view, the prediction is more accurate when non-idealities are counted in the model.

In terms of PMD referred to the attenuation (S12), in the case of vias modelled it ranges between 0.2 and 1% (top-right plot in Fig. 16), while when vias non-idealities are neglected, the same parameter ranges between $\pm 0.6\%$ (top-right plot in Fig. 30). Referring to S21, the PMD

ranges between 0.1 and 0.6% in the top-right plot in Fig. 16, while it spans between -0.6 and 0.1% in the top-right plot in Fig. 30. Further considerations related to the comparison of all the subplots in Figs. 15 and 16, in relation to those in Figs. 29 and 30, are left to the reader.

4.3.6 Configuration 6—sections A_u and A_d activated; sections B, C and D shorted

This configuration is certainly the most interesting in the comparison of the two LEN-based models, as it is the one

Fig. 33 Measured S-parameters characteristics of the RF-MEMS attenuator vs. simulated response (see circuit in Figs. 3, 4, 5) without modelling vertical vias parasitic effects (ideal case), when section A_u is ON, and sections B, C and D are shorted. *Top-left*, reflection (magnitude of S11 parameter); *Top-right*, attenuation (magnitude of S21 parameter); *Bottom-left*, phase of S11 parameter (reflection); *Bottom-right*, phase of S21 parameter (attenuation)

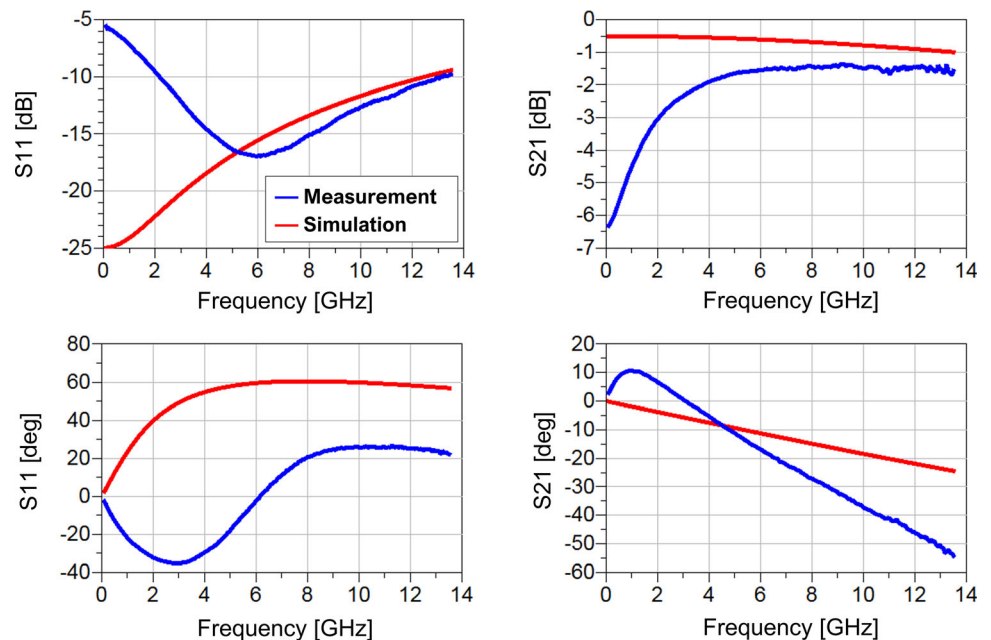
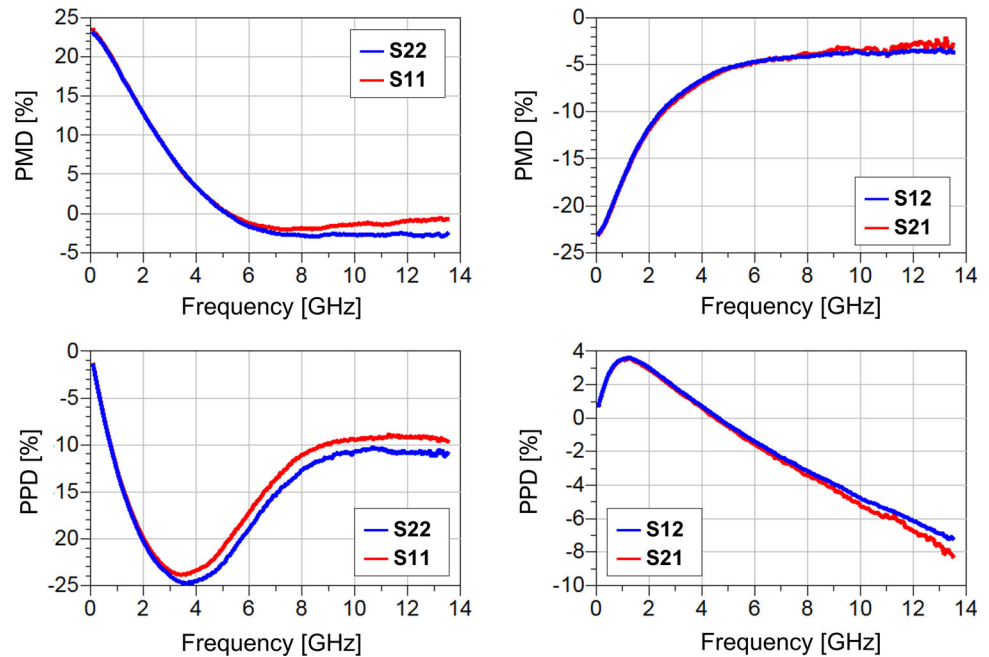


Fig. 34 Measured vs. simulated offsets related to the plots in Fig. 33 (when section A_u is ON, and sections B, C and D are shorted), also including S12 and S22. *Top-left*, PMD of S11 and S22; *Top-right*, PMD of S12 and S21; *Bottom-left*, PPD of S11 and S22; *Bottom-right*, PPD of S12 and S21



with the lowest resistance loading the RF line. The qualitative and quantitative prediction of the attenuation is rather poor in the top-right plot in Fig. 31, while it looks much better in the top-right plot in Fig. 17, when non-idealities are accounted.

In terms of PMD for the attenuation, it ranges between -18 and -3% , both for S12 and S21, in the top-right plot in Fig. 32. Diversely, when vias parasitic effects are modelled, the PMD ranges between -0.7% and around 0.7% , both for the S12 and S21, as visible in the top-right plot in Fig. 18. Also the other parameters show better values when the LEN models vias non-idealities. Further considerations related to the comparison of all the subplots in Figs. 17 and 18, in relation to those in Figs. 31 and 32, are left to the reader.

4.3.7 Configuration 7—section A_u activated; sections B, C and D shorted

This last configuration is rather similar to the previous one, as all the resistors are shorted, while here just one section is activated. The difference is minimal in terms of residual resistance on the RF line. Also in this case, when comparing the plots related to the LEN that models vias non-idealities, in Figs. 19 and 20, with those that neglect the parasitic effects, in Figs. 33 and 34, a large difference in the accuracy of simulations is visible.

Eventually, a few collective considerations are due on the results shown up to here. First, the network under analysis here was intentionally chosen to be rather complex in its geometry and, in turn, in the RF characteristics. This,

in fact, makes more challenging obtaining a trustable description based on LEN approach, and unavoidably pushes towards making some ab-initio choices. In this case, being the studied RF-MEMS a power attenuator, priority in terms of accuracy was given to the attenuation magnitude, i.e., to the S21 parameter. This means that lower error of simulations concerned to the S21 is targeted, at the cost of coarser results for what concerns reflection (S11 and S22) and the corresponding phases.

This said, the goodness of the achieved results can be easily measured comparing the S21 of the LEN accounting for non-idealities of vias, reported from Figs. 7 to 20, against the results for an ideal LEN topology (i.e., neglecting the parasitic effects of vias), reported from Figs. 21 to 34, respectively. In the first group of plots, the simulation S21 exhibits moderate quantitative deviation with respect to measurements, while the qualitative characteristic of the curves is always in good agreement with experiments. On the other hand, in the ideal case, the deviation of LEN simulated curves deviates significantly from experiments, both in quantitative and qualitative terms.

5 Conclusion

MicroElectroMechanical-Systems (MEMS) technology has long been investigated for the production of high-performance, extensively reconfigurable, and tunable Radio Frequency (RF) passive components, commonly referred to as RF-MEMS. Currently, this technology is unlocking new

avenues for exploitation in the emerging application landscapes of Beyond-5th generation mobile communication (B5G) and Future Networks (FN).

This study delves into the technical intricacies surrounding the modeling and simulation of RF characteristics in complex RF-MEMS multi-state networks. Specifically, a reconfigurable step power attenuator is scrutinized. Utilizing experimental datasets obtained from physical samples in various configurations, a Lumped Element Network (LEN) model is developed and fine-tuned. The schematic also incorporates considerations for the surrounding Coplanar Waveguide (CPW) structure, which frames the network and accounts for technology-related non-idealities stemming from the presence of vertical vias. Additionally, it includes the intrinsic bank of resistors implementing a range of attenuation states.

Comparisons and discussions between simulations and experiments are conducted across the frequency spectrum from 100 MHz to 13.5 GHz. Various insights are drawn regarding the accuracy of the LEN model configuration and the impact of the non-idealities integrated into the schematic, both qualitatively and quantitatively, in terms of the behavior of the S-parameters.

Acknowledgements The authors want to acknowledge the sanctioned bilateral project between the National Institute of Technology (NIT) Silchar, India, and Fondazione Bruno Kessler (FBK), Italy (DST sanction no: INT/Italy/P-32/2022 ER), in the frame of the “Executive Programme for Scientific and Technological Cooperation Between the Republic of India and the Italian Republic for the years 2022–2024”, promoted and supported by the Ministry of Science & Technology, Department of Science and Technology, of the Republic of India, and the Ministry of Foreign Affairs, Directorate General for Cultural and Economic Promotion and Innovation—Office IX of the Republic of Italy.

The mentioned project, despite technically focused on Energy Harvesting, provides proper institutional coverage for pursuing joint activities between NIT Silchar and FBK, as the one discussed in this contribution.

Author contributions J.I. wrote the main manuscript, conceptualized the work, and performed the simulations. G.T., Z.M., K.G., S.R.K., I.D.C., and M.D., revised the manuscript and helped improving it.

Data availability No datasets were generated or analysed during the current study.

Declarations

Conflict of interest The authors declare no competing interests.

References

- Brown ER (1997) RF MEMS for digitally-controlled front-end components. *IEEE, Piscataway*. <https://doi.org/10.1109/ICISS.1997.630277>
- Brown ER (1998) RF-MEMS switches for reconfigurable integrated circuits. *IEEE Trans Microw Theory Tech* 46:1868–1880. <https://doi.org/10.1109/22.734501>
- Gad-el-Hak M (2001) *The MEMS Handbook*. CRC Press, Boca Raton. <https://doi.org/10.1201/9780429103872>
- Giacomozzi F, Mulloni V, Colpo S, Iannacci J, Margesin B, Faes A (2011) A flexible fabrication process for RF MEMS devices. *Rom J Inf Sci Technol* 14:259–268
- Goldsmith CL, Yao Z, Eshelman S, Denniston D (1998) Performance of low-loss RF MEMS capacitive switches. *IEEE Microw Guid Wave Lett* 8:269–271. <https://doi.org/10.1109/75.704410>
- Iannacci J (2015) RF-MEMS: an enabling technology for modern wireless systems bearing a market potential still not fully displayed. *Microsyst Technol*. <https://doi.org/10.1007/s00542-015-2665-6>
- Iannacci J (2022) *RF-MEMS technology for high-performance passives* (2nd edition). IOP Publishing, Bristol
- Iannacci J (2023) Modelling, validation and experimental analysis of diverse RF-MEMS ohmic switch designs in view of beyond-5G, 6G and future networks—part 1. *Sensors*. <https://doi.org/10.3390/s23073380>
- Iannacci J, Giacomozzi F, Colpo S, Margesin B, Bartek M (2009) A general purpose reconfigurable mems-based attenuator for radio frequency and microwave applications. In: *IEEE EUROCON 2009, EUROCON 2009*. <https://doi.org/10.1109/EURCON.2009.5167788>
- Iannacci J, Gaddi R, Gnudi A (2010a) Experimental validation of mixed electromechanical and electromagnetic modeling of RF-MEMS devices within a standard IC simulation environment. *J Microelectromechanical Syst* 19:526–537. <https://doi.org/10.1109/JMEMS.2010.2048417>
- Iannacci J, Faes A, Mastro F, Masotti D, Rizzoli V (2010) A MEMS-based wide-band multi-state power attenuator for radio frequency and microwave applications. In: *nanotechnology 2010: electronics, devices, fabrication, MEMS, fluidics and computational-technical proceedings of the 2010 NSTI nanotechnology conference and expo, NSTI-Nanotech 2010*
- Iannacci J, Faes A, Kuenzig T, Niessner M, Wachutka G (2011) Electromechanical and electromagnetic simulation of RF-MEMS complex networks based on compact modeling approach. In: *technical proceedings of the 2011 NSTI nanotechnology conference and expo, NSTI-Nanotech 2011*
- Malczewski A, Eshelman S, Pillans B, Ehmke J, Goldsmith CL (1999) X-band RF MEMS phase shifters for phased array applications. *IEEE Microw Guid Wave Lett* 9:517–519. <https://doi.org/10.1109/75.819417>
- Marcelli R, Bartolucci G, Minucci G, Margesin B, Giacomozzi F, Vitulli F (2004) Lumped element modelling of coplanar series RF MEMS switches. *Electron Lett* 40:1272–1274. <https://doi.org/10.1049/el:20046490>
- Oberhammer J (2017) THz MEMS-micromachining enabling new solutions at millimeter and submillimeter-wave frequencies (invited paper). In: *Asia-Pacific microwave conference proceedings, APMC*. <https://doi.org/10.1109/APMC.2017.8251382>
- Patrick Yue C, Simon Wong S (2000) Physical modeling of spiral inductors on silicon. *IEEE Trans Electron Devices* 47:560–568. <https://doi.org/10.1109/16.824729>
- Pillans B, Eshelman S, Malczewski A, Ehmke J, Goldsmith C (1999) Ka-Band RF MEMS phase shifters. *IEEE Microw Guid Wave Lett* 9:520–522. <https://doi.org/10.1109/75.819418>
- Shah U, Decrossas E, Jung-Kubiak C, Reck T, Chattopadhyay G, Mehdi I, Oberhammer J (2015) 500–600 GHz submillimeter-wave 3.3 bit RF MEMS phase shifter integrated in micromachined waveguide. In: *2015 IEEE MTT-S international microwave symposium, IMS 2015* <https://doi.org/10.1109/MWSYM.2015.7166829>

- Shah U, Reck T, Frid H, Jung-Kubiak C, Chattopadhyay G, Mehdi I, Oberhammer J (2017) A 500–750 GHz RF MEMS waveguide switch. *IEEE Trans Terahertz Sci Technol* 7:326–334. <https://doi.org/10.1109/TTHZ.2017.2670259>
- Shen SC, Feng M (1999) Low actuation voltage RF MEMS switches with signal frequencies from 0.25GHz to 40GHz. Technical digest-international electron devices meeting. IEEE, Piscataway
- Tilli M, Motooka T, Airaksinen VM, Franssila S, Paulasto-Kröckel M, Lindroos V (2015) Handbook of silicon based MEMS materials and technologies: second edition. Elsevier, Amsterdam
- Uttamchandani D (2013) Handbook of mems for wireless and mobile applications. Woodhead Publishing Limited, Sawston. <https://doi.org/10.1533/9780857098610>
- Yammouch T, Okada K, Masu K (2008) Physical modeling of MEMS variable inductor. *IEEE Trans Circuits Syst II Express Briefs* 55:419–422. <https://doi.org/10.1109/TCSII.2007.914443>
- Yao JJ (2000) RF MEMS from a device perspective. *J Micromechanics Microengineering* 10:R9–R38. <https://doi.org/10.1088/0960-1317/10/4/201>

Publisher's Note Springer Nature remains neutral with regard to jurisdictional claims in published maps and institutional affiliations.

Springer Nature or its licensor (e.g. a society or other partner) holds exclusive rights to this article under a publishing agreement with the author(s) or other rightsholder(s); author self-archiving of the accepted manuscript version of this article is solely governed by the terms of such publishing agreement and applicable law.